

# Electrochemical CO<sub>2</sub> Reduction into Chemical Feedstocks: From Mechanistic Electrocatalysis Models to System Design

Md Golam Kibria, Jonathan P. Edwards, Christine M. Gabardo, Cao-Thang Dinh, Ali Seifitokaldani, David Sinton, and Edward H. Sargent\*

The electrochemical reduction of CO<sub>2</sub> is a promising route to convert intermittent renewable energy to storable fuels and valuable chemical feedstocks. To scale this technology for industrial implementation, a deepened understanding of how the CO<sub>2</sub> reduction reaction (CO<sub>2</sub>RR) proceeds will help converge on optimal operating parameters. Here, a techno-economic analysis is presented with the goal of identifying maximally profitable products and the performance targets that must be met to ensure economic viability—metrics that include current density, Faradaic efficiency, energy efficiency, and stability. The latest computational understanding of the CO<sub>2</sub>RR is discussed along with how this can contribute to the rational design of efficient, selective, and stable electrocatalysts. Catalyst materials are classified according to their selectivity for products of interest and their potential to achieve performance targets is assessed. The recent progress and opportunities in system design for CO<sub>2</sub> electroreduction are described. To conclude, the remaining technological challenges are highlighted, suggesting full-cell energy efficiency as a guiding performance metric for industrial impact.

## 1. Introduction

Beginning with the industrial revolution, increasing combustion of fossil fuels has led to an escalation in atmospheric CO<sub>2</sub> concentrations. These CO<sub>2</sub> emissions trap solar energy within the Earth's atmosphere and contribute to climate change. If global CO<sub>2</sub> emissions continue to rise, the Earth is expected to warm 4 °C above pre-industrial levels.<sup>[1–3]</sup> The projected effects of global warming include increased likelihood of extreme weather events, reduced food security, increased competition for fresh water, and

species extinction.<sup>[4]</sup> In response to these projections, a recent global summit on climate change held in Paris in 2015 agreed to take the steps required to limit the temperature rise in this century to below 2 °C.<sup>[5]</sup> To limit global warming to these levels, society needs to find means to reduce the rate of global CO<sub>2</sub> emissions.<sup>[1–3,6,7]</sup>


One approach to reduce atmospheric CO<sub>2</sub> emissions is to capture CO<sub>2</sub> and sequester or utilize it. Utilization includes the conversion of CO<sub>2</sub> into value-added products via electrochemical CO<sub>2</sub> reduction reaction (CO<sub>2</sub>RR). This method, which has recently attracted increased research attention,<sup>[8,9]</sup> has several advantages. The increased deployment of renewable energy sources, such as wind and solar, is leading to an increasingly variable power supply, calling for an improved means of energy storage to avoid the curtailment of excess

power.<sup>[10–13]</sup> CO<sub>2</sub>RR can be scaled to facilitate the large-scale storage of these renewable electrons in the form of chemical products. Since the products of CO<sub>2</sub>RR—chemicals and liquid fuels—are today derived from petrochemical sources, their production via CO<sub>2</sub>RR could reduce global demand for fossil fuels.<sup>[14–16]</sup> Additionally, certain CO<sub>2</sub>RR products are in high demand, and thus provide avenues to market adoption.<sup>[9,17–19]</sup> Liquid fuels produced via CO<sub>2</sub>RR can be distributed using the existing energy infrastructure, increasing the speed with which renewable-powered CO<sub>2</sub> electroreduction can have impact.<sup>[20–23]</sup>

This review examines the upgrading of CO<sub>2</sub> to chemical feedstocks via electrochemical conversion. We present a techno-economic analysis (TEA) to determine which CO<sub>2</sub>RR products are most attractive from an economic point of view, and which operating parameters have the greatest impact on overall feasibility. Reaction pathways leading to the products of particular interest are highlighted. We also discuss ways in which improved models of electrocatalytic reactions could advance mechanistic understanding of CO<sub>2</sub>RR and inform better catalyst designs. Next, we discuss the state-of-the-art electrocatalysts and the material engineering techniques employed to enhance their performance. We then examine electrolyzer design and identify the system level parameters such as reactor configuration, electrolyte, pressure, and temperature that govern performance. We conclude by proposing promising routes to advance CO<sub>2</sub> electrolyzers toward industrial adoption.

Prof. M. G. Kibria,<sup>[†]</sup> Dr. C.-T. Dinh, Dr. A. Seifitokaldani, Prof. E. H. Sargent  
Department of Electrical and Computer Engineering  
University of Toronto  
10 King's College Road, Toronto, Ontario M5S 3G4, Canada  
E-mail: ted.sargent@utoronto.ca

J. P. Edwards, Dr. C. M. Gabardo, Prof. D. Sinton  
Department of Mechanical and Industrial Engineering  
University of Toronto  
5 King's College Road, Toronto, Ontario M5S 3G8, Canada

 The ORCID identification number(s) for the author(s) of this article can be found under <https://doi.org/10.1002/adma.201807166>.

<sup>[†]</sup>Present address: Department of Chemical and Petroleum Engineering, University of Calgary, 2500 University Drive NW, Calgary, Alberta T2N 1N4, Canada

DOI: 10.1002/adma.201807166

## 2. Techno-Economic Analysis of CO<sub>2</sub>RR

Techno-economic analysis can be used to evaluate the feasibility of the CO<sub>2</sub> conversion process, target economically promising products, and identify the performance metrics that must be achieved to reach economic viability.

### 2.1. Products

Based on the number of electrons transferred during the reaction, CO<sub>2</sub>RR can produce up to 16 different gas and liquid products, albeit with a wide range of selectivities.<sup>[24]</sup> Two-electron-transfer products, such as carbon monoxide (CO) and formate (HCOO<sup>-</sup>, or formic acid in acidic media, HCOOH), are readily achieved on a variety of catalysts with high selectivity. Multiple-electron-transfer products, including methanol, methane, ethanol (C<sub>2</sub>H<sub>5</sub>OH), ethylene (C<sub>2</sub>H<sub>4</sub>), and propanol (C<sub>3</sub>H<sub>8</sub>O), have so far been produced with lower selectivity. In addition to carbon-based products, the parasitic hydrogen evolution reaction (HER) can also occur and compete for reaction electrons.

### 2.2. Market Size and Price

Market size is critical in terms of both commercial potential and ultimate CO<sub>2</sub> utilization potential. In this regard, methane, methanol, ethanol, and ethylene are promising products, with each having a market size larger than 80 million tons (Mt) per year (Figure 1a). Methane is the major constituent of natural gas and a precursor for various chemicals. Methanol and ethanol are used as solvents, precursors, and directly as fuels. Ethylene is an important precursor for the polymer industry, especially in the synthesis of polyethylene, the most widely used plastic globally.<sup>[25]</sup>

Another important consideration for targeted CO<sub>2</sub>RR products is the market price (US\$ t<sup>-1</sup>). Ethanol and ethylene are good targets compared to methanol and methane in view of their higher market price per ton (Figure 1a). Price is often normalized to the chemical energy stored (equal to the thermodynamic energy required to produce the chemicals from CO<sub>2</sub>RR, measured in cents kWh<sup>-1</sup>, herein termed energy value) to enable comparison of products requiring different electrical energy input (Figure 1b). This analysis makes CO, formate, and propanol promising targets. In addition, ethanol and ethylene boast moderate energy values and remain attractive targets due to their large market size.

### 2.3. System Analysis

The levelized cost of the CO<sub>2</sub>RR products considers both capital and operational costs. Capital costs are derived from CO<sub>2</sub> electrolyzer hardware, whereas operational costs arise from the electricity use, CO<sub>2</sub> feedstock, and product separation costs.

#### 2.3.1. CO<sub>2</sub> Electrolyzer Cost

We leverage the analogy between CO<sub>2</sub> and water electrolyzers for an initial estimate of CO<sub>2</sub> electrolyzer cost, in the absence



**Md Golam Kibria** is an Assistant Professor in the Department of Chemical and Petroleum Engineering at University of Calgary, Canada. He is interested in heterogeneous catalysis, system design, and techno-economic analysis for sustainable synthesis of renewable fuels and feedstocks, including electro/photocatalysis for CO<sub>2</sub> reduction and water splitting for sustainable energy and environment.



**David Sinton** is a Professor and Canada Research Chair in Microfluidics and Energy at the University of Toronto. He is currently an NSERC E.W.R. Steacie Memorial Fellow, before which he was the Associate Chair of Research in Mechanical & Industrial Engineering, and the Interim Vice-Dean of research in the Faculty of Applied Science. He is a cofounder and Chief Technology Officer of Interface Fluidics Ltd. He received his B.Sc. degree from the University of Toronto, M.Eng. degree from McGill University, and Ph.D. degree from the University of Toronto.



**Edward H. Sargent** holds the rank of University Professor in the Edward S. Rogers Sr. Department of Electrical and Computer Engineering at the University of Toronto. He holds the Canada Research Chair in Nanotechnology and also serves as Vice-President, International, for the University of Toronto. His research focuses on renewable energy harvesting and storage with nanomaterials, including quantum dots for efficient, low-cost solar energy harvesting solutions and catalysts for conversion of CO<sub>2</sub> to fuel.

of commercial CO<sub>2</sub> electrolyzers operating at large scales. In this TEA, we use an electrolyzer cost of \$5000–15 000 m<sup>-2</sup>, a range seen in proton-exchange membrane (PEM) water electrolyzers.<sup>[17]</sup>

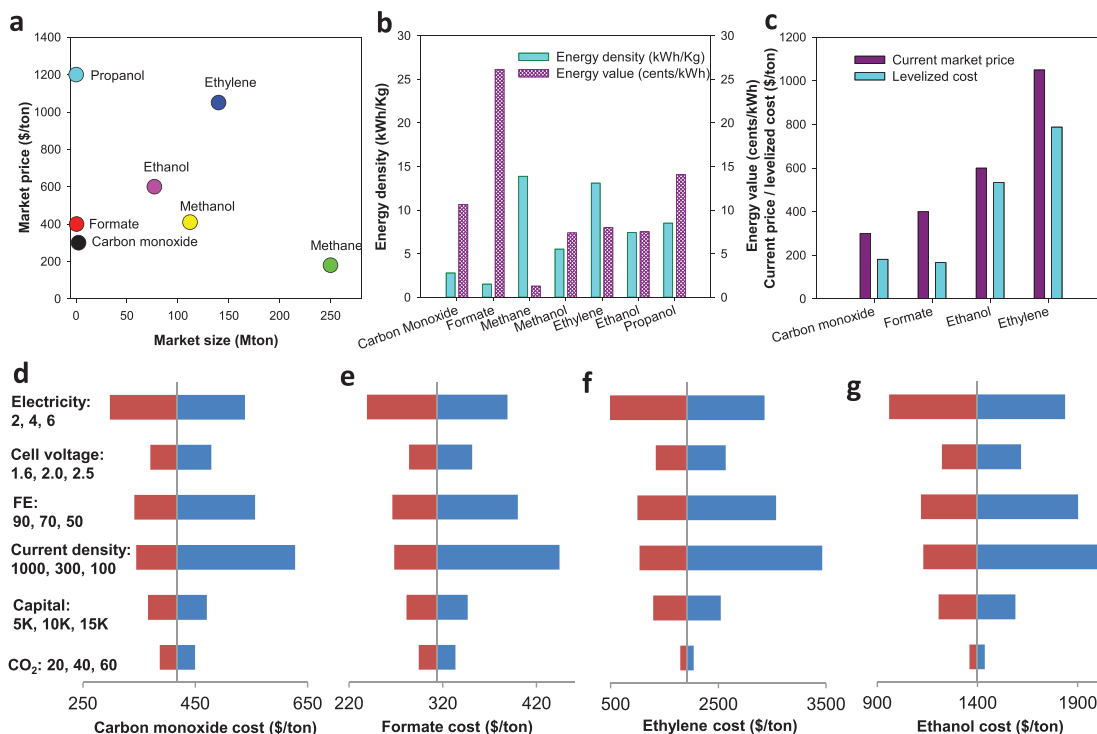


**Figure 1.** CO<sub>2</sub>RR product market and TEA. a) Market size (Mt) and market price (\$ t<sup>-1</sup>) of common CO<sub>2</sub>RR products. b) Energy stored (kWh kg<sup>-1</sup>) in the CO<sub>2</sub>RR products and their energy values (current market price per energy unit). c) Comparison between market price and levelized production cost for CO, formate, ethanol, and ethylene. The levelized cost was calculated based on the following assumptions: CO<sub>2</sub> cost: \$40 t<sup>-1</sup>; electrolyzer cost: \$5000 m<sup>-2</sup>; electricity price: 2 cents kWh<sup>-1</sup>; cell voltage: 1.8 V; Faradaic efficiency: 90%; and current density: 500 mA cm<sup>-2</sup>. d–g) Dependence of levelized cost for: d) CO, e) formate, f) ethylene, and g) ethanol on the electricity price (cents kWh<sup>-1</sup>), cell voltage (V), Faradaic efficiency (%), current density (mA cm<sup>-2</sup>), capital cost (electrolyzer, \$ m<sup>-2</sup>), and CO<sub>2</sub> cost (\$ t<sup>-1</sup>). The numbers below each parameter correspond to (from left to right) high performance, base case, and low performance, respectively.

### 2.3.2. Operational Cost

As in hydrogen production from water electrolysis, electricity costs are the determining factor for the economic feasibility of CO<sub>2</sub>RR products in most techno-economic models.<sup>[17–19,26,27]</sup> Due to their higher energy requirements, products containing more C–H and C–C bonds, such as ethylene and ethanol, are more sensitive to electricity prices compared to CO and formate, assuming similar energy efficiency (EE) and selectivity (Figure 1d–g). For example, when the electricity price increases 2 cents, the electroproduction cost of CO and formate increases 25%, while that of ethylene and ethanol increases over 33%. With renewable electricity from wind and solar becoming less expensive, the Department of Energy’s (DOE) target is 2–3 cents kWh<sup>-1</sup> in 2030.<sup>[28]</sup> These cost reductions, in combination with CO<sub>2</sub>RR performance improvements, will improve the economics of CO<sub>2</sub>RR (Figure 1c).

The cost associated with the CO<sub>2</sub> feedstock is dependent on the CO<sub>2</sub> capture method. CO<sub>2</sub> captured from concentrated CO<sub>2</sub> sources, such as power and chemical plants and using amine technology, has the lowest price of \$50–70 t<sup>-1</sup> with a DOE target of \$40 t<sup>-1</sup> in the 2020–2025 time frame.<sup>[29]</sup> Capturing CO<sub>2</sub> from air is more expensive than that from flue gas because of its low concentration: a recent study showed that the cost for CO<sub>2</sub> capture from air could potentially reach ≈\$100–200 t<sup>-1</sup> in the future.<sup>[29]</sup> In this work, we use a CO<sub>2</sub> cost of \$40 t<sup>-1</sup> for our TEA.

### 2.3.3. Separation Cost

In CO<sub>2</sub>RR, gas separation is required because of the presence of unconverted CO<sub>2</sub> in the gas product stream, as well as the generation of unintended products. In addition, liquid product separation is often required to extract products contained in the liquid catholyte. For gas product separation, pressure swing adsorption (PSA) and membrane technologies are currently being used in other industrial processes with similar gas compositions.<sup>[30]</sup> Pressure swing is generally preferred in CO<sub>2</sub>RR product separation because of low operating costs and high efficiency. In this work, we use a separation cost of \$10 t<sup>-1</sup>, which is similar to other CO<sub>2</sub>RR TEAs based on industrial biogas separation with PSA technology<sup>[18]</sup> and the Sherwood plot for the separation of dilute streams.<sup>[19]</sup> The capital costs associated with separation are not included in this study.

Liquid product separation can be achieved through distillation, extraction, precipitation, and pervaporation.<sup>[30]</sup> Among these methods, distillation is the most widely used approach because the main liquid CO<sub>2</sub>RR products are alcohols. Compared to gas separation using PSA, liquid separation exhibits a similar capital cost, but a much higher operational cost.<sup>[18]</sup> Based on the Sherwood plot, a separation cost of \$60 t<sup>-1</sup> of liquid product is estimated assuming a minimum input of 10 wt% product concentration.<sup>[19]</sup> Similarly, we apply a separation cost of \$60 t<sup>-1</sup> for liquid products.

## 2.4. Performance Targets for the CO<sub>2</sub>RR

In CO<sub>2</sub>RR, several figures of merit are used to characterize process performance, including current density, Faradaic efficiency (FE), energy efficiency (EE), and stability.

### 2.4.1. Current Density

The current density in CO<sub>2</sub>RR reflects the rate of the reaction. In practical applications, a geometric current density, which is defined as the current flow per geometric area (i.e., top-view area, rather than physical surface area, which can be much higher) of the electrode, is used. The current density directly affects the capital cost because it governs the size of the electrolyzer needed for a given production rate. Using a base case capital cost of \$920 m<sup>-2</sup> for an alkaline electrolyzer configuration, Jouny et al. estimated that a current density of 250–300 mA cm<sup>-2</sup> can enable a viable CO<sub>2</sub>RR process. Increasing the current density to 500 mA cm<sup>-2</sup> only slightly changed the profit margin.<sup>[18]</sup> When a PEM electrolyzer configuration with an assumed capital cost of \$15 000 m<sup>-2</sup> was used, the current density needed to be much higher than 300 mA cm<sup>-2</sup> to make the conversion of CO<sub>2</sub> to ethanol economically viable.<sup>[26]</sup> In this study, we found that the production cost significantly increases when the current density decreases from 300 to 100 mA cm<sup>-2</sup> (Figure 1d–g) and only slightly decreases when the current density increases from 300 to 1000 mA cm<sup>-2</sup>. Thus, a high current density (usually >300 mA cm<sup>-2</sup>) is required to minimize capital investment for a desired CO<sub>2</sub>RR production rate.

### 2.4.2. Faradaic Efficiency

The FE reflects the selectivity of the current toward a specific CO<sub>2</sub>RR product. A high FE minimizes separation requirements and reduces the total current required for a target production rate. As shown in Figure 1d–g, the production costs for all products show a strong dependence on FE.<sup>[18]</sup>

### 2.4.3. Energy Efficiency

The EE is the percentage of the energy stored in the desired products compared to the total energy input needed to synthesize them. The EE of an electrolyzer is calculated via the product of the FE and the voltage efficiency. The voltage efficiency is the thermodynamic cell voltage divided by the actual cell voltage (the sum of the thermodynamic voltage, reaction overpotentials, and cell losses). The total electricity cost is dependent on the electricity price (cents kWh<sup>-1</sup>) and the amount of electricity used which is proportional to the EE and the product energy value. The levelized cost of the products of interest is sensitive to both the electricity price and EE (Figure 1d–g), indicating that electricity requirements are a significant portion of the CO<sub>2</sub>RR product cost. For example, in the case of ethanol and ethylene (Figure 1f,g), when the electricity price increases 50% (from 4 to 6 cents kWh<sup>-1</sup>), the production cost increases more than 30%, indicating that the electricity cost accounts for more

than 60% of the product cost. While the electricity price may be subject to many external factors, the EE of the system can be optimized to reduce total electricity requirements. This goal can be achieved by increasing the FE and lowering the cell voltage. Our TEA (Figure 1c) shows that with an FE of 90% and a cell voltage of 1.8 V, the production costs for several products are lower than current market price, making their production from CO<sub>2</sub>RR profitable provided these metrics are achieved.

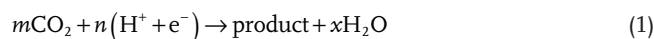
### 2.4.4. Stability

The CO<sub>2</sub> electrolyzer must meet the preceding performance targets (current density, FE, and EE) over a prolonged period of time. For reference, industrial water electrolyzers have demonstrated over 80 000 h of stable performance.<sup>[19]</sup> Long-term stability is crucial for reducing maintenance and replacement costs, as well as associated electrolyzer downtime. Employing less expensive electrolyzer components, namely inexpensive catalysts and gas diffusion layers, may further lessen the stability requirement. However, long-term CO<sub>2</sub>RR has not been well studied, with most of the reports showing a very short testing time (usually <100 h). It is noted that high CO<sub>2</sub>RR stability requires durability from all components of the electrolyzer (discussed in Section 5).

In summary, based on market prices and performance metrics, CO and formate appear the most promising target products for CO<sub>2</sub>RR. However, low energy density (Figure 1b), limited market of pure CO and formate (Figure 1a), and challenges with storage and transportation have been the key issues in widespread large-scale production of these chemicals. With their larger market size and higher energy density, long-chain hydrocarbons and oxygenate liquid products, such as ethylene and ethanol respectively are therefore promising targets to address the issues associated with CO and formate production. As outlined in our TEA, achieving the target performance metrics of current density (>300 mA cm<sup>-2</sup>), FE (80–90%), cell voltage (<1.8 V), and stability (>80 000 h) is required to make these products economically viable.

## 3. Computational Insight into the Reaction Mechanisms

CO<sub>2</sub>RR is a reaction with multiple proton–electron transfer steps leading to carbon-based products and water



There are three types of bond formation steps in CO<sub>2</sub>RR: oxygen hydrogenation (O–H), carbon hydrogenation (C–H), and carbon–carbon coupling (C–C). There are two proposed mechanisms for hydrogenation: the Eley–Rideal mechanism, in which H<sub>2</sub>O and e<sup>-</sup> are the reactants; and the Langmuir–Hinshelwood mechanism, in which catalyst surface adsorbed hydrogen (\*H) is the reactant.

Experimental conditions can be simulated computationally to explore reaction mechanisms. Quantum chemistry calculations consider electron transfer in chemical reactions by



calculating the electron structure of the reactants and products. Among different methods developed for quantum chemistry calculations, density function theory (DFT) efficiently calculates the reaction energetics based on the adsorption energies of different reaction intermediates. The calculated reaction energies have an uncertainty of 0.1 eV. However, describing all the complexities of the electrochemical interface within the DFT model, with respect to the number and the type of components (catalyst, solvent molecules, solvent ions, etc.), as well as the physics and chemical implications (electric fields, solvation, free energy, charge transfer, etc.), is challenging due to computational limitations. Early DFT computations assumed that the reaction took place in vacuum, without explicitly considering the water molecules in aqueous electrolytes or the electric field induced by the ions. To include solvation effects, such as hydrogen bonding, the adsorption energies calculated in this approach were corrected by 0.1 eV for CO and CHO, 0.45 eV for OH, and 0.25 eV for R–OH, where R denotes a hydrocarbon.<sup>[31–33]</sup> However, later studies revealed inaccuracies in calculating reaction energies in this approach,<sup>[34–38]</sup> resulting from the omission of electric field and solvation effects during the simulation. To address these inaccuracies, explicit and implicit solvation models were developed. The explicit solvation model considers the electrolyte in the simulation, allowing it to be more representative of experimental conditions. However, this model requires more computational resources and time compared to the implicit solvation model, which estimates the dielectric of the electrolyte and its effects on chemical bindings based on the Boltzmann–Poisson equation in the continuum solvent model.

The combination of the proton-coupled electron-transfer (PCET) model with the computational hydrogen electrode model provides means of determining the chemical potential of protons and electrons by avoiding the explicit treatment of solvated protons.<sup>[39]</sup> In this model, protons and electrons are paired so that their collective chemical potential is equal to half of the chemical potential of gaseous hydrogen ( $H_2$ ) at a potential of 0 V and pH 0. This approach is widely used to calculate reaction energy barriers of hydrogenation steps as a function of applied potential; however, it does not model nonelectrochemical steps, nor can it simulate steps involving only electrons or only protons. Moreover, in the PCET model, changes in pH are not reflected in changes on the reversible hydrogen electrode (RHE) scale.

The electrochemical charge transfer barrier can be modeled either under constant voltage or constant current. Simulations under constant voltage mimic real experimental conditions in which metallic catalysts are poised at a specific potential, but this approach requires a hypothetically infinite model system with computationally expensive boundary conditions. Although simulations at a constant current require a relatively small cell size, this approach can lead to dramatic potential shifts ( $\approx 2$  V) due to the changes in the interfacial charge density along the reaction path. Different models have been proposed,<sup>[40]</sup> considering explicit<sup>[41]</sup> and implicit water,<sup>[34–37]</sup> a charged water layer,<sup>[42]</sup> a solvated proton and surface with excess electrons,<sup>[43,44]</sup> and surface hydrogenation,<sup>[45,46]</sup> to provide either constant voltage simulation in a regular unit cell size or constant current simulation without dramatic shifts in surface potential.

### 3.1. CO and Formate Formation

CO and formate are the simplest products of  $CO_2RR$ , needing only two proton–electron pairs. The selectivity of these products depends on the initial binding mode of the first intermediate of  $CO_2$  reduction, i.e.,  $*COOH$  or  $*HCOO$  (Figure 2, orange and green pathways, respectively), where  $*$  indicates the atom bound to the catalyst. The carboxyl intermediate ( $*COOH$ ), believed to be formed through a PCET step (in which the proton ( $H^+$ ) and electron ( $e^-$ ) simultaneously transfer to the adsorbed species), leads to CO formation by further hydrogenation and dehydration. A detailed study at pH 7 was performed by Cheng et al. using an explicit water model to study the CO formation pathway.<sup>[38]</sup> In contrast with previously proposed models, CO formation was shown to proceed from physisorbed  $CO_2$  to chemisorbed  $CO_2$  ( $*CO_2^{\delta-}$ ), with a free energy barrier of 0.43 eV (Figure 2, top orange pathway). Lower subsequent barriers of  $*CO_2^{\delta-}$  hydrogenation to form  $*COOH$  (0.37 eV) and the dissociation of  $*COOH$  to form  $*CO$  (0.30 eV) were calculated. In this report, chemisorbed  $*CO_2^{\delta-}$  species was stabilized through the hydrogen bond network and was considered as a reaction intermediate, not just a transition state.

Formate is formed through the  $*HCOO$  intermediate, which is bound to the surface via both oxygen atoms, leaving the C atom available for hydrogenation. This hydrogenation step involves either a surface hydrogen ( $*H$ ) or a solvated proton ( $H^+$ ) (Figure 2, green pathways). Electrolyte pH regulates the availability and source of hydrogen for this step. A recent study showed that hydrogenation via surface hydrogen is favored because the C–H bond is less polar as compared to the O–H bond.<sup>[47]</sup> In addition, formate formation was shown to proceed through the direct surface protonation along with electron transfer to the physisorbed  $CO_2$ .<sup>[38]</sup> Thus, the competition between CO and formate formation occurs in the first electron-transfer step.

### 3.2. $C_1$ versus $C_2$ Product Formation

CO is considered a key intermediate in the formation of multicarbon hydrocarbons and oxygenates from  $CO_2RR$  because similar product distributions result from the direct reduction of CO. These two reactions exhibit similar potential dependencies, further suggesting that the rate-determining step occurs after CO formation.<sup>[48,49]</sup> When activation energy barriers and solvation effects are omitted, CO hydrogenation to formyl ( $*CHO$ ) is considered the rate-determining step, and ethylene is formed by the dimerization of  $*OCH_x$  species and subsequent deoxygenation.<sup>[32,50,51]</sup> However, experiments indicate a limiting step common in methane and ethylene formation that is not included in this mechanism.<sup>[52]</sup> When explicit water is included in the simulation, calculations of the potential-dependent activation energy for the transition state suggest that CO hydrogenation proceeds through the  $*COH$  intermediate.<sup>[41,42]</sup> The subsequent  $*COH$  hydrogenation steps result in the  $*CH_x$  intermediate on the catalyst surface, which was considered as a common precursor for both methane and ethylene formation. Although this mechanism is in better agreement with experimental results, it contradicts



hydrogenation steps in the ethylene pathway proceed through the Eley–Rideal mechanism with the protons provided by water molecules. At  $-0.69$  V versus RHE, the binding energy of surface protons is increased, matching the CO binding energy and resulting in the competition of  $*\text{H}$  and  $*\text{CO}$  for surface sites. Higher surface proton availability at potentials less than  $-0.85$  V versus RHE leads to  $*\text{CHO}$  formation, altering the mechanism for ethylene production from exclusively CO dimerization (which does not require surface hydrogen) to the  $*\text{CO}$  and  $*\text{CHO}$  coupling mechanism (activation energy barrier of  $0.71$  eV).<sup>[34]</sup> At even more negative potentials, the HER activation energy barrier is lowered, thereby causing a decrease in the coverage of adsorbed hydrogen due to their consumption in this parasitic reaction. However, at these extremely negative potentials, the activation energy barrier for C–C bond formation increases, causing the CO dimerization pathway to shut down and the methane formation pathway to proceed through the  $*\text{CHOH}$  intermediate.<sup>[34]</sup> These findings suggest that working in the potential range of  $-0.6$  to  $0.85$  V is beneficial for ethylene formation.

The effects of other reaction conditions on CO dimerization have also been studied. For example, when increasing  $*\text{CO}$  coverage, it has been shown that  $*\text{CO}$  binding energy significantly decreases due to the adsorbate–adsorbate lateral repulsion,<sup>[58]</sup> and consequently,  $*\text{CO}$  dimerization improves.<sup>[33]</sup> Simultaneously,  $*\text{H}$  adsorption becomes more difficult, and the overpotential for HER increases. Moreover, cation-induced electric fields have been shown to reduce the  $*\text{CO}$  dimerization barrier.<sup>[33]</sup> Another study demonstrated that cation-induced electric fields and solvation effects together significantly reduce both free and activation energies for  $*\text{CO}$  dimerization.<sup>[42]</sup> Furthermore, strain within a catalyst material can change the electronic structure and coordination, which in turn changes the reaction energetics and modulates catalyst selectivity.<sup>[59–61]</sup> Previous DFT studies have shown that tensile strain improves the  $*\text{CO}$  dimerization by increasing the adsorption energy of CO and consequently increasing CO surface coverage and suppresses the competing HER.<sup>[33,62]</sup> Thus, by altering the reaction environment through increased electric fields (e.g., larger cations in the electrolyte), increased CO coverage (e.g., higher  $\text{CO}_2$  pressure), and/or increased catalyst strain (e.g., engineering a core–shell structure<sup>[63]</sup>), it is possible to improve the catalytic activity toward multicarbon products.

Overall, DFT calculations are a helpful tool for understanding  $\text{CO}_2\text{RR}$  mechanisms. Many improvements have been made to the predictive capability of DFT, but further advances are necessary to model the complexities of multicarbon product formation. With the inclusion of all electrochemical system parameters in DFT models, it will be easier to navigate the various C–C coupling mechanisms and multicarbon pathways currently proposed. Knowing the mechanistic picture can help suggest strategies to shut down unwanted pathways and improve the selectivity toward the desired products.

### 3.3. High-Throughput Computations and Microkinetic Models

DFT calculations are computationally demanding and cannot practically provide detailed large-scale screening of

catalysts and conditions. The ability to predict the reaction energetics based on a few simple descriptors would enable high-throughput computations to optimize catalytic materials while decreasing the total number of DFT calculations. Similarities in the chemical bonds between adsorbed species at different catalytic surfaces suggest a universal scaling relation. Specifically, adsorption energies of carbon-bound species and oxygen-bound species have been correlated to the adsorption energy of  $*\text{CO}$  and  $*\text{OH}$ , respectively.<sup>[64]</sup> In this case, the limiting potentials of each elementary step were estimated based on the surface affinity for  $*\text{CO}$  and  $*\text{OH}$ . Similarly, in another study, the adsorption energies of  $\text{CO}_2\text{RR}$  intermediates, such as  $*\text{COOH}$ ,  $*\text{COH}$ , and  $*\text{CHO}$ , were scaled versus the  $*\text{CO}$  binding energy on close-packed transition metals.<sup>[58]</sup> These relations provide useful descriptors for high-throughput computations in search of materials with greater catalytic activities. For instance, high-throughput DFT simulations were used to screen Ag-based catalysts for efficient CO production.<sup>[65]</sup> It was found that p-block dopants modulate reaction energetics by imposing partial covalency into the Ag catalyst, thereby enhancing catalytic activity.

The complexity of accurate electrochemical models does not allow for high-throughput computational screening of the large parameter space of  $\text{CO}_2\text{RR}$  variables. Using machine learning, one can leverage the ever-growing datasets for the adsorption energies of different reaction intermediates on different catalysts, to train models for predicting more active and selective  $\text{CO}_2\text{RR}$  catalysts without running massive DFT computations in a large variable space, including catalyst type, reactants, and reaction environment. There are a few recent studies using machine learning to explore the complex reaction network,<sup>[66]</sup> find active bimetallic facets for  $\text{CO}_2\text{RR}$ ,<sup>[67]</sup> or identify alloys for  $\text{CO}_2\text{RR}$  and HER,<sup>[68]</sup> but this tool has great promise to aid in the design of next-generation, highly active catalyst materials.

DFT computations calculate the reaction free energy and activation energy barrier for each elementary step along a reaction pathway. From these calculations, the onset potential and the potential-determining step can be ascertained. The onset potential is useful in determining the catalytic activity toward a certain reaction. However, microkinetic models are needed to use the DFT calculated activation energy barriers to determine the reaction rates, the catalytic activity, the product distribution, and the current density under real experimental conditions. Several microkinetic models on Ag<sup>[69]</sup> and Cu<sup>[34]</sup> have been proposed, but further work is needed to produce comprehensive models capable of accurately predicting the  $\text{CO}_2\text{RR}$  product distribution under different applied potentials, pH, electrolyte concentrations, partial pressures, and temperatures.

## 4. Catalysts for $\text{CO}_2$ Electroreduction

Over the last few decades, several catalysts have been explored to reduce the activation energy barrier for  $\text{CO}_2\text{RR}$ . The ability of a catalyst to reduce the energy barrier depends on the binding energies of specific reaction intermediates along the pathway to the different  $\text{CO}_2\text{RR}$  products, thereby directly influencing the final product distribution. As a result, electrocatalyst materials

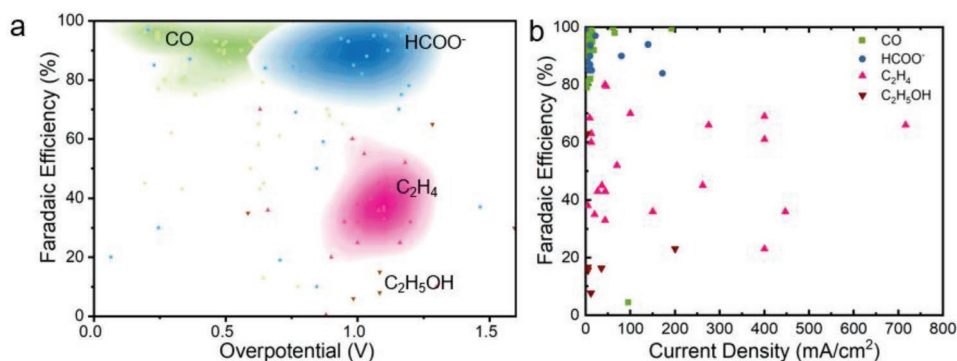


**Figure 3.** Summary of CO<sub>2</sub>RR performance. a) Kernel density estimation of Faradaic efficiency and corresponding overpotential; the background color intensity represents the density of data points. b) Maximum Faradaic efficiency and its corresponding current density.<sup>[18,70–76]</sup>

can be divided into three main groups based on their tendency to bind various CO<sub>2</sub> reaction intermediates and generate certain products. Group 1 catalysts weakly bind the \*CO<sub>2</sub><sup>δ-</sup> intermediate, resulting in the selective production of formate. Group 2 catalysts bind with the \*CO<sub>2</sub><sup>δ-</sup> intermediate and the following \*COOH intermediate strong enough for subsequent reduction to \*CO. Weak binding of the \*CO intermediate results in the production of CO from group 2 catalysts. Finally, group 3 catalysts bind to all the previously mentioned intermediates, including \*CO, and can further reduce the \*CO intermediate to form multicarbon products, including hydrocarbons and oxygenates. **Figure 3** summarizes performance achieved for the products of interest determined by the TEA using CO<sub>2</sub>RR catalysts from groups 1 to 3.

#### 4.1. Selective Production of Formate

Group 1 catalysts include p-block metals (e.g., Sn, In, Pb, Ti, Hg, Cd, and Bi) that are selective for formate production. Strategies such as structuring and catalyst doping have been employed to improve the selectivity of these catalyst materials. For example, Zheng et al. reported a threefold enhancement in formate selectivity using a sulfur-modulated Sn catalyst (Sn(S)/Au) as compared to a Sn nanoparticle/Au catalyst,<sup>[77]</sup> which was attributed to the S-induced undercoordinated sites of the Sn nanoparticles. The Sn(S)/Au catalyst exhibited an FE<sub>HCOO<sup>-</sup></sub> up to 93% at -0.75 V versus RHE for over 40 h. Recently, García de Arquer et al. demonstrated a 2D Bi-based catalyst derived from a BiOBr template for highly selective (>90% FE) and stable CO<sub>2</sub> reduction at 200 mA cm<sup>-2</sup>.<sup>[75]</sup> In situ grazing-incidence wide-angle X-ray scattering and X-ray absorption spectroscopy (XAS) studies reveal that the preferential exposure of highly active Bi (110) facets in this oxyhalide-derived catalyst is the source of the high selectivity.

Apart from the p-block metal catalysts, a few other catalysts show great promise for formate production at low overpotentials. Gao et al. reported a partially oxidized Co four-atomic layer catalyst that achieved FE<sub>HCOO<sup>-</sup></sub> up to 90% at -0.24 V versus RHE for over 40 h.<sup>[78]</sup> The Tafel slope of 44 mV per decade suggested the enhanced CO<sub>2</sub> adsorption capability of the layered catalyst accelerated CO<sub>2</sub> activation. In addition, Pd has produced formate at low overpotentials, but CO poisoning of the catalyst has limited stable operation.<sup>[79]</sup> To circumvent the

CO poisoning effect, Klinkova et al. synthesized Pd nanoparticles containing an abundance of high-index facets and surface kinks to weaken the CO binding affinity.<sup>[80]</sup> This catalyst was stable for over 6 h and was able to achieve an FE >90% at -0.2 V versus RHE. Alternatively, metal-free catalysts, such as boron-doped diamond, have been able to attain an FE<sub>HCOO<sup>-</sup></sub> >90% during 24 h of stable operation.<sup>[81]</sup> Although promising, further in situ studies are required to clarify the mechanistic origins of these highly selective metal-free catalysts. In brief, CO<sub>2</sub>RR to formate has achieved the target performance metrics (i.e., overpotential, current density) to be economically viable. Although it has the highest energy value (Figure 1b), limited industrial use of formate (Figure 1a) has been the key hindrance for its widespread industrial production via CO<sub>2</sub>RR.

#### 4.2. Selective Production of CO

With their selective production of CO, the most common group 2 electrocatalyst materials include Au and Ag, which have weak binding of the \*CO intermediate.<sup>[82]</sup> Several nanostructuring strategies have been reported to enhance the selectivity and reduce the overpotential of Au and Ag, by increasing their surface area, edge sites, strain, or low-coordinated sites. For example, Liu et al. designed a catalyst that significantly boosted local electric fields, enhancing the local concentration of electrolyte cations (**Figure 4a**) and CO<sub>2</sub>, through ultrasharp nanoneedle structuring of Au (**Figure 4b**).<sup>[76]</sup> Tafel analysis showed faster kinetics of the first electron transfer for the Au nanoneedles as compared to Au nanorods and Au nanoparticles. As a result, the authors attained high FE (>95%) and current density (22 mA cm<sup>-2</sup>) for CO generation with very low overpotential (0.24 V) using Au nanoneedles (**Figure 4c**). Similarly, performance enhancements have been reported on oxide-derived (OD) nanostructured Ag catalyst.<sup>[83]</sup> OD catalysts prepared by electrochemically reducing Ag<sub>2</sub>O demonstrated higher activity for CO<sub>2</sub>RR to CO than polycrystalline Ag. The OD Ag required 0.49 V less overpotential than polycrystalline Ag (0.89 V) to achieve an FE<sub>CO</sub> of 80%. The reduction in overpotential is attributed to the OD Ag's low-coordination surface sites, which enhance the stabilization of the \*COOH intermediate. Moreover, OD Au catalysts, prepared by electrochemically reducing a thick Au oxide film, can also exhibit a high FE<sub>CO</sub> (>96%) at



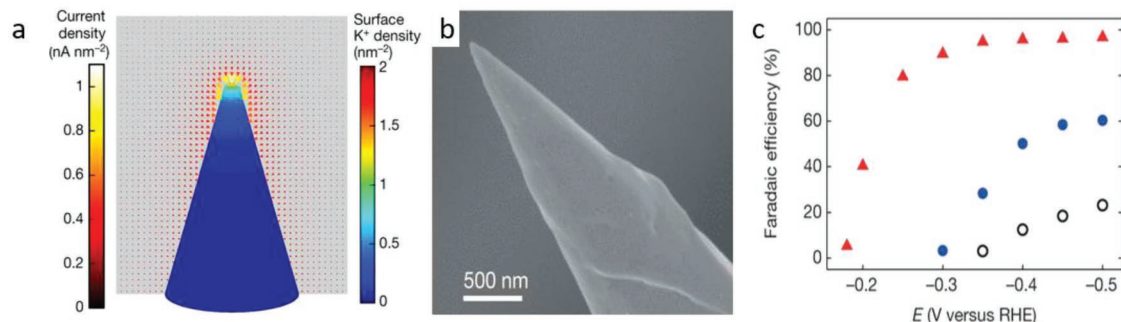


**Figure 4.** a) Surface K<sup>+</sup> density and current density distributions on the surface of Au needles. The tip radius is 5 nm. b) Scanning electron microscopy (SEM) image of Au nanoneedles. c) CO Faradaic efficiencies on Au nanoneedles (red), Au nanorods (blue), and Au nanoparticles (black) at different applied potentials.<sup>[76]</sup> a–c) Reproduced with permission.<sup>[76]</sup> Copyright 2016, Springer Nature.

low overpotentials (0.24 V) compared to their polycrystalline Au counterparts (Figure 5a).<sup>[84]</sup> Further studies on OD Au demonstrated a large presence of grain boundaries (GBs), which was linearly correlated with surface-area-normalized activity for CO<sub>2</sub>RR (Figure 5b).<sup>[85]</sup> Recently, Mariano et al. verified the high CO<sub>2</sub>RR selectivity for GBs using scanning electrochemical cell microscopy.<sup>[86]</sup> It was revealed that GBs create catalytically active strained regions in polycrystalline Au by stabilizing dislocations. Distinct from dislocation-induced strain effects, GBs may also create high step densities that are catalytically active for the CO<sub>2</sub>RR. Atomistic modeling has revealed a deeper understanding of the catalytic activity of GB on Au surfaces, including broken scaling relations<sup>[87]</sup> and broken local spatial

symmetry near the GB.<sup>[88]</sup> In summary, OD nanostructuring of the catalyst has been demonstrated to be an effective strategy to enhance the activity and reduce the overpotential for CO production. However, the current understanding of the key underlying mechanism is inconclusive and requires further study.

Apart from structural effects, a number of reports have highlighted the effect of adsorbed species on CO<sub>2</sub>RR activity to CO. For instance, Hsieh et al. fabricated a Ag nanocoral electrocatalyst in the presence of aqueous chloride anions that demonstrated an FE<sub>CO</sub> of 95% at an overpotential of 0.37 V.<sup>[89]</sup> The presence of chloride ions on the surface of Ag nanocorals more than doubles the FE<sub>CO</sub> as compared to chloride-free Ag nanocorals. Analogous effects pertaining to adsorbed chloride

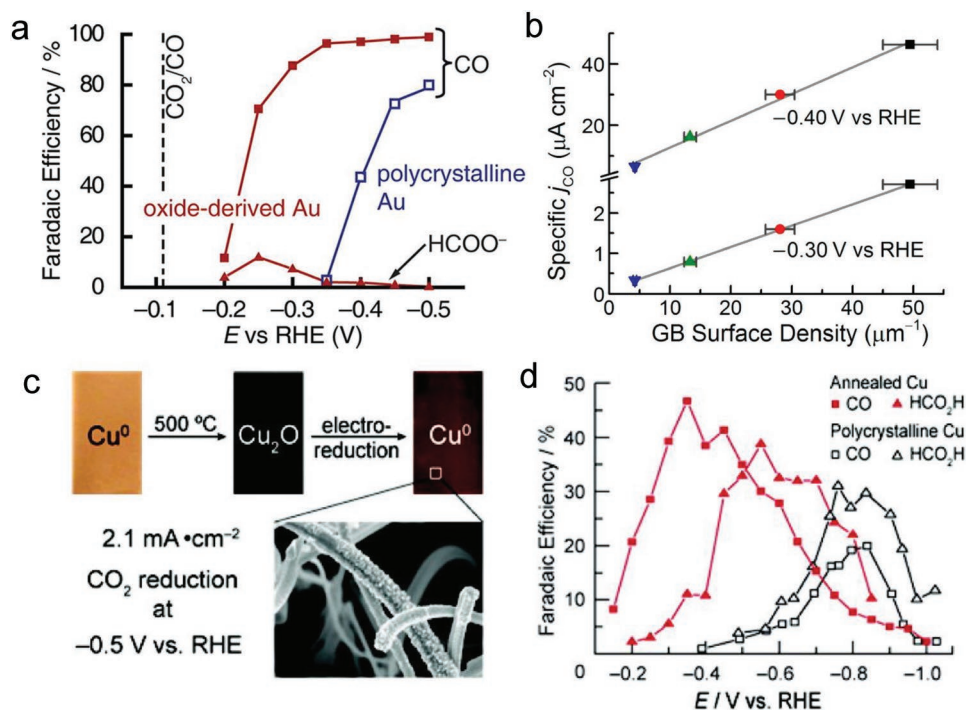


**Figure 5.** a) FEs for CO and formate production on oxide-derived Au and polycrystalline Au electrodes at various potentials between -0.2 and -0.5 V in 0.5 M NaHCO<sub>3</sub>, pH 7.2. Dashed line indicates the CO equilibrium potential. a) Reproduced with permission.<sup>[84]</sup> Copyright 2012, American Chemical Society. b) Measured specific partial current for CO and GB surface density in Au nanoparticle on carbon nanotubes at low overpotentials. b) Reproduced with permission.<sup>[85]</sup> Copyright 2015, American Chemical Society. c) Schematic of the oxidation–reduction process of Cu foil. d) FE for CO and HCOOH versus applied potential. c,d) Reproduced with permission.<sup>[104]</sup> Copyright 2012, American Chemical Society.

and cyanide anions have been observed on Au electrodes.<sup>[90,91]</sup> Likewise, the introduction of small organic molecules on the surface of Ag nanoparticles was reported to be an effective way to improve the CO<sub>2</sub>RR activity.<sup>[92]</sup> Detailed DFT studies suggest the attachment of amine molecules to Ag nanoparticles destabilizes hydrogen binding, and thereby suppresses HER.<sup>[92]</sup> Further in operando studies may elucidate the role of adsorbed species in enhancing selectivity, thereby assisting in the rational design of catalyst-adsorbed species combinations for selective CO production.

Looking beyond the common group 2 electrocatalyst materials, low-cost transition-metal single-atom catalysts (SACs) have been successfully employed in numerous other catalytic reactions<sup>[93,94]</sup> and have recently emerged as promising catalysts for CO production due to their high activity, selectivity, and high atomic efficiency.<sup>[95–99]</sup> For example, theoretical studies suggest that the single atomic sites of Ni, as compared to metallic Ni, possess a different electronic structure that facilitates CO<sub>2</sub>RR to CO and suppresses the competing HER.<sup>[100]</sup> While SACs offer compelling performance opportunities in CO<sub>2</sub>RR, economical and large-scale synthesis techniques have posed a grand challenge for implementing these CO<sub>2</sub>RR materials in industrial settings. Very recently, Zheng et al. demonstrated an inexpensive, facile, and scalable synthesis protocol for Ni SACs on commercial carbon black that exhibited an FE<sub>CO</sub> of nearly 100% at current densities above 100 mA cm<sup>-2</sup>.<sup>[96]</sup> Such results are encouraging and demonstrate the need for further studies to elucidate the unique role of SACs in order to guide rational design and synthesis of new SACs for CO<sub>2</sub>RR.

In an effort to reduce catalyst expense, metal-free carbon-based materials have received attention due to their electrocatalytic activity for CO<sub>2</sub>RR.<sup>[70]</sup> Wu et al. reported a nitrogen-doped carbon nanotube (NCNT) catalyst that obtained an FE<sub>CO</sub> of 80% at an overpotential of 0.26 V.<sup>[101]</sup> This performance was attributed to an optimum binding energy, yielding strong \*COOH adsorption and \*CO desorption. Further studies on NCNTs revealed that the catalytic activity is very dependent on the density and type of nitrogen defect.<sup>[102]</sup> In a separate study, nitrogen defect-incorporated 3D graphene exhibited superior activity as compared to Ag and Au, achieving an FE of 85% at a lower overpotential of 0.47 V.<sup>[103]</sup> Pyridinic N is found to be the most active site in carbon matrix for CO<sub>2</sub>RR as reported in a number of studies. In general, the development of metal-free carbon-based materials for CO<sub>2</sub>RR is promising owing to their tailored porous structure, high resistance to acids and bases, high-temperature stability, and environmental friendliness. Heteroatom (e.g., S, N, B, etc.) doping has shown great potential in enhancing the selectivity of metal-free carbon-based materials. Elucidating the exact active sites in carbon matrices may aid in the rational design of highly selective catalysts toward the products of interest.

In summary, great progress has been made in the production of CO from CO<sub>2</sub>RR with the reported selectivity, current density, and overpotential exceeding the minimum performance targets for economic viability, making it likely the first target product for large-scale CO<sub>2</sub> electrolyzers. Considering the fact that pure CO does have a small market (Figure 1a), it would be worth pursuing a two-step tandem electrochemical system wherein the produced CO can further be electrochemically

reduced to more energy value fuels.<sup>[26,105]</sup> Alternatively, a downstream process (e.g., Fischer–Tropsch or fermentation)<sup>[26,106]</sup> can be pursued in conjunction with CO<sub>2</sub> electrolysis to upgrade CO.

### 4.3. Selective Production of Multicarbon Products

As the only metal catalyst in group 3, Cu can produce up to 16 different products,<sup>[24]</sup> including various hydrocarbons and alcohols, due to its ability to bind and further reduce the \*CO intermediate. In a recent study, Dinh et al. demonstrated that thermally deposited Cu nanoparticle can exhibit ~83% selectivity toward C<sub>2+</sub> products, with ethylene (66%) the primary product at 275 mA cm<sup>-2</sup> and –0.54 V versus RHE.<sup>[74]</sup> This result indicates that unmodified Cu can be highly selective for C<sub>2+</sub> products.

Due to the variety of possible products, many strategies have been explored to tune the product selectivity on Cu including morphological and compositional modifications of the catalysts. Similar to Au and Ag, a number of studies have explored the use of OD Cu for the enhancement of CO<sub>2</sub>RR activity at lower overpotential (Figure 5c,d).<sup>[104,107,108]</sup> While high selectivity toward multicarbon products has been demonstrated on OD Cu<sup>[109,110]</sup> at low overpotentials, the underlying mechanism is yet to be well understood, and is often attributed to crystallite sizes and facets, strains, GBs, and an increased local pH. A number of works have reported that the OD Cu catalyst possesses an abundance of GBs, shown to be strong CO-binding sites, enabling these catalysts to be highly active in CO reduction to multicarbon products.<sup>[105,111–113]</sup> However, the specificity of GBs toward multicarbon products has not been well understood. Lum and Ager recently studied OD Cu, reducing mixtures of <sup>13</sup>CO and <sup>12</sup>CO<sub>2</sub> to reveal the product specificity of GBs. Interestingly, the authors were able to identify at least three different active sites in OD Cu which are selective to ethylene, ethanol/acetate, and 1-propanol, respectively.<sup>[114]</sup> The unique catalytic activity of OD Cu has also been attributed to internal strain.<sup>[111]</sup> The presence of microstrain in GB-rich Cu nanoparticles was revealed using transmission electron microscopy (TEM) studies and Williamson–Hall analysis of the X-ray diffraction patterns. However, it remains unclear how such a small amount (<0.2%) of microstrain in the GB-rich Cu can significantly alter the binding energy of the reaction intermediates.

Differences in the oxidation state of Cu are another potential factor that may alter CO<sub>2</sub>RR activity.<sup>[92,93]</sup> For example, Handoko et al. reported selective reduction of CO<sub>2</sub> to ethane and ethanol on thick OD Cu electrodes, which they attributed to the stabilization of \*CH<sub>3</sub> intermediates by Cu<sup>+</sup>.<sup>[110]</sup> Various studies<sup>[115,116]</sup> have utilized bulk-sensitive in situ X-ray absorption near-edge structure spectroscopy to show that Cu<sup>+</sup> is stable during the course of CO<sub>2</sub>RR, a finding recently supported by another study using in situ soft XAS measurements (Figure 6a,b).<sup>[117]</sup> These findings enable high selectivity toward C<sub>2</sub> products to be attributed to the residual Cu<sup>+</sup>.<sup>[116]</sup>

In contrast to the above reports on the crucial role of Cu<sup>+</sup>, other groups have reported that Cu<sup>+</sup> is rapidly reduced and remains as Cu<sup>0</sup> under reducing conditions.<sup>[118]</sup> For example, using surface-sensitive in situ Raman spectroscopy with selected-ion flow tube mass spectrometry, Mandal et al. did

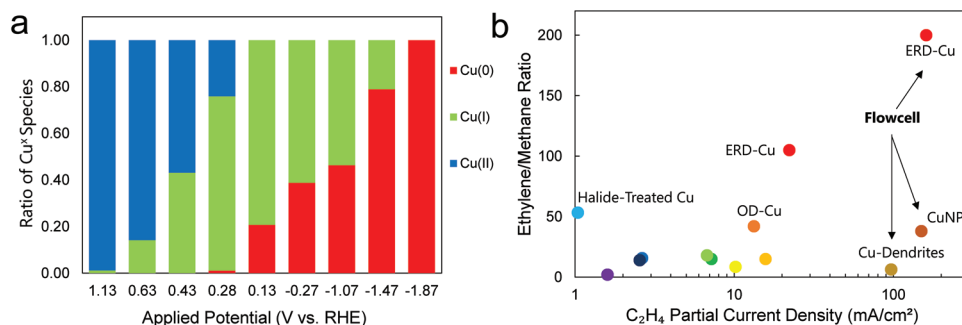


**Figure 6.** a) Calculated ratio of Cu oxidation states from linear combination of soft XAS spectra fitted to the Cu L<sub>3</sub>-edge spectra versus applied potential. b) Plot of ethylene/methane ratio versus ethylene partial current density for a range of catalysts. a,b) Reproduced with permission.<sup>[117]</sup> Copyright 2018, Springer Nature.

not detect CO<sub>2</sub>RR products as long as Cu<sub>2</sub>O was present at the catalyst surface (Figure 7).<sup>[119]</sup> Their DFT studies suggested that the reduction of Cu<sub>2</sub>O is favored both kinetically and energetically over CO<sub>2</sub>RR. In another work, the stability of residual oxides was investigated by synthesizing <sup>18</sup>O-enriched OD Cu catalysts and measuring the <sup>18</sup>O content via ex situ secondary-ion mass spectrometry measurements.<sup>[120]</sup> Only <1% of the original <sup>18</sup>O content remained after only ≈10 min of reaction at −1.0 V versus RHE, indicating that residual oxides are unstable in OD Cu catalysts. Eilert et al. recently performed in situ ambient pressure X-ray photoelectron spectroscopy (XPS) and TEM electron energy loss spectroscopy to reveal the presence of residual surface oxygen (e.g., Cu<sub>2</sub>O or Cu(OH)<sub>2</sub>) and trapped subsurface oxygen during reaction.<sup>[121]</sup> On the catalyst surface, pure metallic phase Cu was revealed; however, the presence of subsurface oxygen was correlated with higher C<sub>2</sub> selectivity, with the enhancement attributed to changes in the electronic structure of the Cu that enhance the binding of \*CO. DFT studies further support that subsurface oxygen enhances the adsorption energy, and consequently, the surface coverage of \*CO on Cu (100).<sup>[122]</sup> As a result, the probability of CO dimerization is increased, which is the rate-determining step toward C<sub>2</sub> products. Moreover, Cavalca et al. determined that the stabilization of subsurface oxygen under the reaction conditions is possible due to the abundant defects present in the OD Cu electrodes.<sup>[123]</sup> In contrast to the above reports, a few other DFT studies reveal that subsurface oxygen has negligible effect on the CO<sub>2</sub>RR activity of Cu.<sup>[124,125]</sup> In general, the conclusions drawn from bulk-sensitive techniques support the

presence of residual Cu<sup>+</sup> in OD Cu catalysts, which is credited with the enhanced CO<sub>2</sub>RR activity. On the other hand, surface-sensitive techniques have been used to conclude that there is no residual Cu<sup>+</sup> and the enhanced performance of OD Cu may result from subsurface oxygen. Thus, it remains inconclusive whether residual surface oxide and/or subsurface oxygen are responsible for the enhanced catalytic activity of OD Cu catalyst. To elucidate this ambiguity, future studies may involve studying the catalytic activity of atomically thin Cu and partially oxidized Cu sheets with and without surface Cu oxide, similar to studies on partially oxidized atomic Co layers.<sup>[78]</sup>

Cu-based metal alloys have also garnered interest due to their ability to tune product selectivity by modulating the stability of key reaction intermediates. In one report, Hoang et al. created an electrodeposited Cu–Ag alloy, containing 6% Ag, which demonstrated FEs for C<sub>2</sub>H<sub>4</sub> and C<sub>2</sub>H<sub>5</sub>OH of nearly 55% and 26%, respectively, at a cathode potential of −0.7 V versus RHE.<sup>[126]</sup> In situ Raman revealed the origin of the high selectivity to be the optimum availability of the \*CO intermediate and the enhanced stabilization of the Cu<sub>2</sub>O overlayer. Lee et al. used an electrochemical codeposition technique to create phase-blended Ag-incorporated biphasic Cu<sub>2</sub>O–Cu catalysts. The Ag-doped phase-blended catalysts exhibited a threefold higher ethanol selectivity (FE<sub>C<sub>2</sub>H<sub>5</sub>OH</sub> = 34.15%) than that of the Cu<sub>2</sub>O without Ag dopant (10.5%). The Ag–Cu biphasic boundaries were thought to suppress HER and increase \*CO mobility from Ag to Cu sites.<sup>[127]</sup> Ren et al. tuned the Zn content in a series of OD Cu<sub>x</sub>Zn catalysts to achieve an FE<sub>C<sub>2</sub>H<sub>5</sub>OH</sub> of 29.1%.<sup>[128]</sup> Further, Ma et al. reported high selectivity (>60%) toward C<sub>2</sub> chemicals using phase-separated

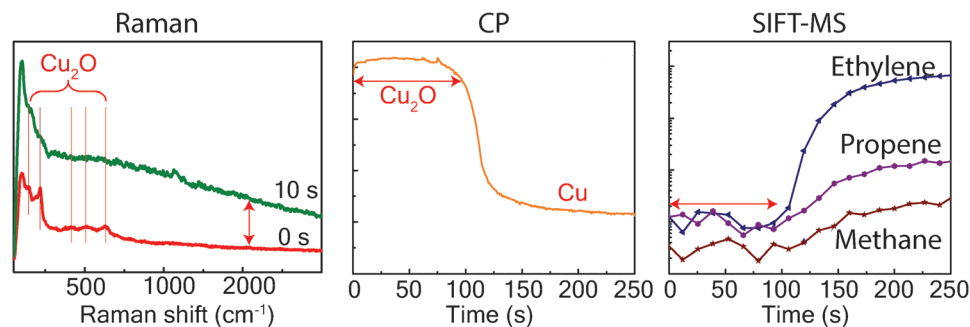


**Figure 7.** Left: Raman spectra of Cu oxide before (red) and after CO<sub>2</sub>RR (green); middle: chronopotentiometry curve of Cu oxide; right: selected-ion flow tube mass spectrometry curves showing the evolution of different products over time. Reproduced with permission.<sup>[119]</sup> Copyright 2018, American Chemical Society.



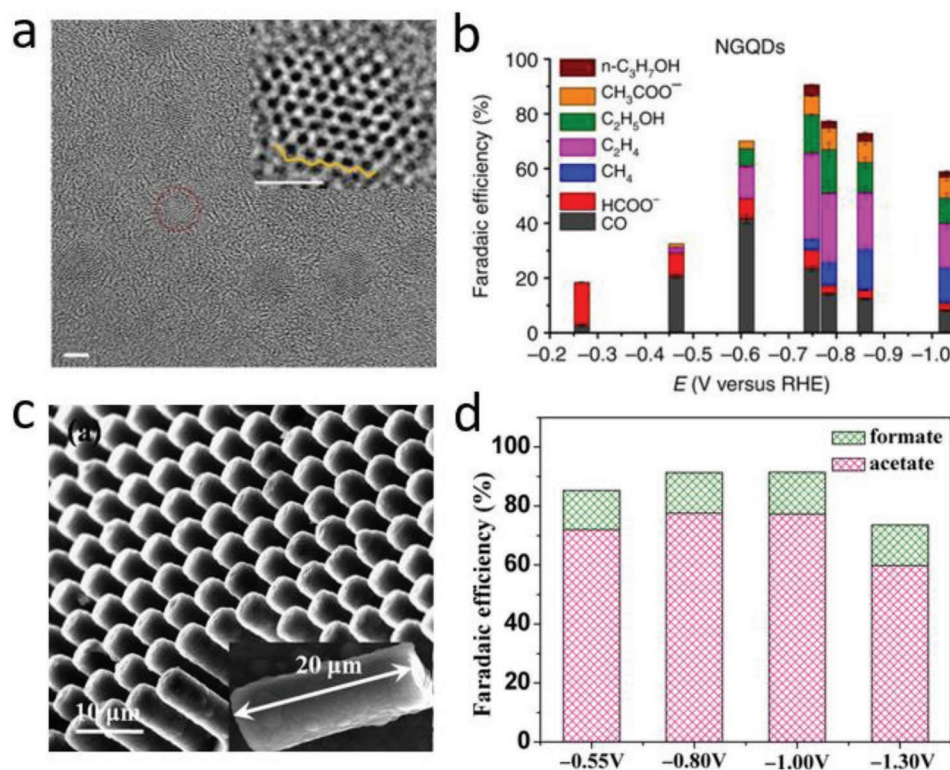


**Figure 8.** a) High-magnification TEM image of N-doped graphene quantum dots. Scale bar: 2 nm. Inset shows a single N-doped graphene quantum dot containing zigzag edges as circled. The yellow line outlines the zigzag edge. Scale bar in inset: 1 nm. b) FEs of carbon monoxide (CO), methane (CH<sub>4</sub>), ethylene (C<sub>2</sub>H<sub>4</sub>), formate (HCOO<sup>-</sup>), ethanol (EtOH), acetate (AcO<sup>-</sup>), and *n*-propanol (*n*-PrOH) at various applied cathodic potentials for N-doped graphene quantum dots. a,b) Reproduced under the terms of the CC-BY Creative Commons Attribution 4.0 International License (<http://creativecommons.org/licenses/by/4.0/>).<sup>[133]</sup> Copyright 2016, The Authors, published by Springer Nature. c) SEM images of N-doped nanodiamond/Si rod array. d) FE for acetate and formate production for CO<sub>2</sub>RR on a N-doped nanodiamond/Si rod array electrode at -0.55 to -1.30 V versus RHE. c,d) Reproduced with permission.<sup>[135]</sup> Copyright 2015, American Chemical Society.

CuPd alloys.<sup>[129]</sup> The geometric arrangements of the Cu and Pd rather than the electronic effect were reported to be the key in tuning the product selectivity. In addition, Xu et al. found that the incorporation of Au not only stabilizes Cu nanoparticles, but also lowers the overpotential for CO<sub>2</sub>RR.<sup>[130]</sup> Jia et al. reported an electrodeposited Cu–Au alloy (Cu<sub>63.9</sub>Au<sub>36.1</sub>), which exhibited an alcohol selectivity of 28% in contrast to 5% on the bulk Cu catalyst.<sup>[131]</sup> Kim et al. performed a systematic study on bimetallic Cu–Au nanoparticle monolayers and concluded that synergistic electronic and geometric effects govern the binding energies of the key intermediates along the alcohol pathway.<sup>[132]</sup> In brief, rationally designed Cu-based metal alloys have shown great promise in enhancing the selectivity of CO<sub>2</sub>RR toward multicarbon alcohols.

Metal-free carbon electrode materials have also been reported for CO<sub>2</sub>RR to hydrocarbons and oxygenates.<sup>[70]</sup> Jingjie et al. reported a N-doped graphene quantum dot catalyst with a selectivity toward ethylene and ethanol of 45%. The high selectivity was attributed to the synergistic effect of the nanostructuring, yielding highly exposed edge sites, and the heteroatom N doping (Figure 8a,b).<sup>[133]</sup> Liu et al. reported a B and N codoped nanodiamond catalyst, with very high ethanol selectivity (FE of 93.2%) at -1.0 V versus RHE.<sup>[134]</sup> The combination of B and N codoping and the balance between the N content and H<sub>2</sub> evolution potential were key for achieving high ethanol selectivity. Liu et al. reported that nitrogen-doped nanodiamond

(NDD) can serve as a promising catalyst for the formation of acetate (Figure 8c,d).<sup>[135]</sup> Faradaic efficiency of 92% for acetate production has been demonstrated at -0.8 to -1.0 V versus RHE. Based on the XPS analysis, the authors reasoned the high activity to the presence of N–sp<sup>3</sup> C active sites as well as high overpotential for HER on NDD catalyst.

While significant progress has been made in synthesizing Cu- and carbon-based catalysts for multicarbon products, to date the reported performance is well below the performance targets to ensure economic viability, especially with respect to current density and EE. However, it is worth pursuing systematic further studies on Cu-based metal alloys and carbon materials, since cooperative and synergistic effects of different materials may lead to further enhancements of overall performance.

Developing and demonstrating novel CO<sub>2</sub>RR catalyst materials increasingly rely upon parallel innovation in system design to optimize the reaction environment (i.e., electrolyte, temperature, pressure). The main system architectures and the opportunities they present are discussed in the following sections.

## 5. System Design for CO<sub>2</sub> Electroreduction

Many CO<sub>2</sub>RR studies have focused on catalyst development and optimization, with most of the performance testing conducted



in traditional H cell reactors. In this configuration, the reacting  $\text{CO}_2$  is dissolved in the liquid electrolyte. Such reactors make use of common carbon electrode substrates, such as glassy carbon or carbon paper, allowing for simple catalyst deposition and rapid screening of various catalysts. The stability of these systems is generally on the order of tens of hours. Given the simplicity of the experimental system, the measured performance can usually be directly attributed to the catalyst, albeit within the limitations of H cell conditions. In H cells, the current density is limited (typically under  $100 \text{ mA cm}^{-2}$ ) by the available  $\text{CO}_2$  dissolved in the electrolyte, which is only  $34 \times 10^{-3} \text{ M}$  at room temperature.<sup>[136]</sup> However, as highlighted in our TEA, the current density must be greater than  $300 \text{ mA cm}^{-2}$  for industrial application. Thus, alternative electrolyzer architectures are being pursued for large-scale implementation. Inspiration for these flow cell designs comes from water electrolyzers, a similar electrochemical technology to  $\text{CO}_2$  electrolyzers that have scaled efficiently to meet commercial demands.

### 5.1. Electrolyzer Types

Inspired by water electrolyzers, three main architectures have emerged for  $\text{CO}_2$  electrolyzers: liquid-phase, gas-phase, and solid oxide electrolyzers (Figure 9). With  $\text{CO}_2\text{RR}$  taking place on the cathode of each type of reactor, the anode reaction is the well-studied oxygen evolution reaction (OER) borrowed from water electrolyzers. A summary of these electrolyzer architectures is presented in Table 1 with each configuration outlined below.

#### 5.1.1. Liquid-Phase Electrolyzer

A common flow cell architecture is the liquid-phase electrolyzer, similar to alkaline electrolyzers. It consists of three flow channels, one for each of the  $\text{CO}_2$  gas, catholyte, and anolyte as shown schematically in Figure 9. A gas diffusion electrode separates the catholyte and gas channel. The catalyst layer, located on the liquid facing front of the gas diffusion electrode, contacts the electrolyte while gas-phase  $\text{CO}_2$  is continuously delivered to the catalyst through the back of the gas diffusion electrode. The catholyte and anolyte liquid streams are separated by an ion-exchange membrane, which

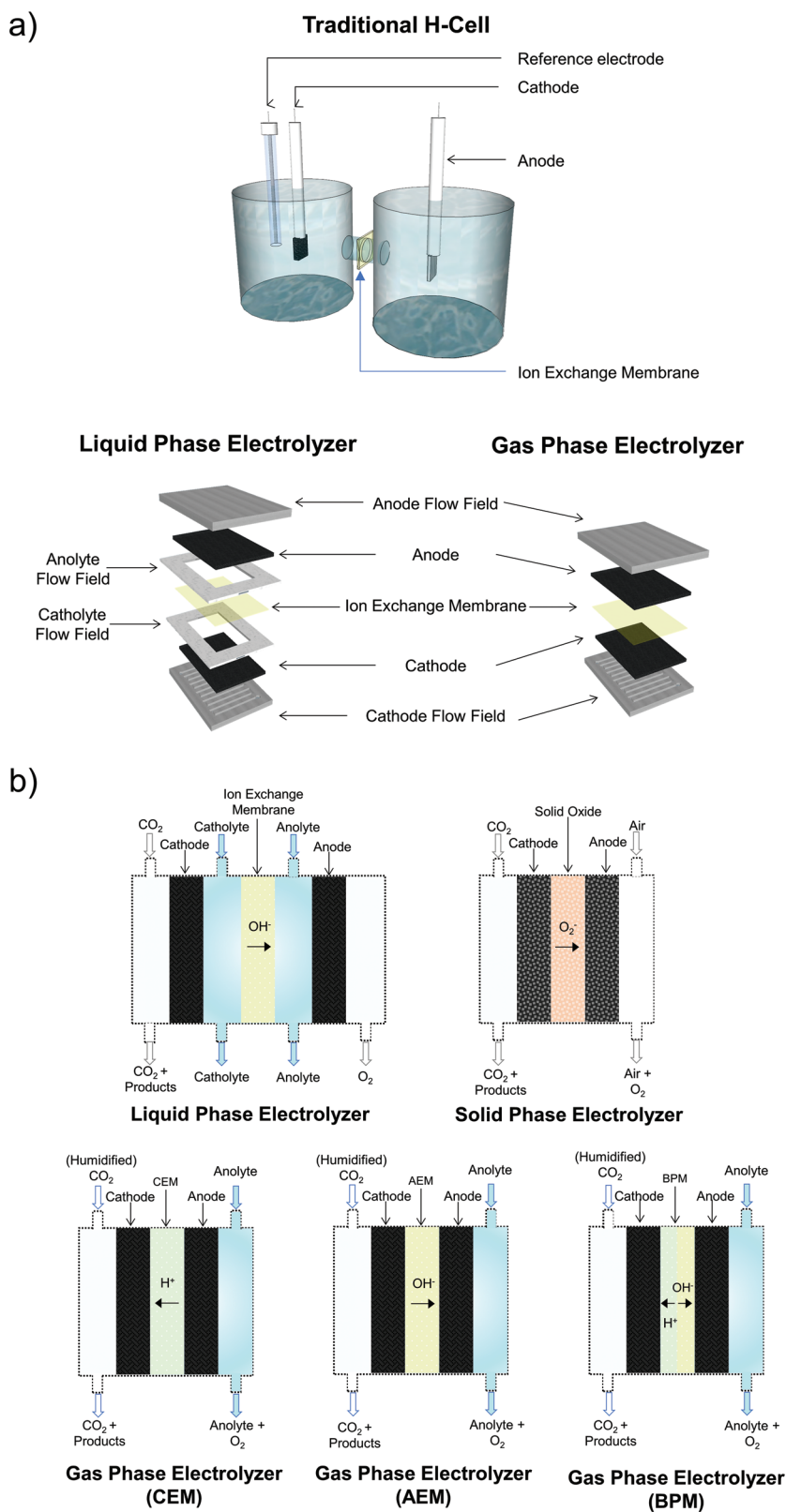


**Figure 9.** a) Schematics of various electrolyzer types: traditional H cell, liquid-phase electrolyzer, and gas-phase electrolyzer. b) Cross-sectional view of the liquid-phase, solid-phase, and gas-phase (CEM, AEM, BPM) electrolyzers.

**Table 1.** Comparison of the different architectures employed in CO<sub>2</sub> electrolyzers.

Reactor structure	Type	Operating conditions			Maximum current	Advantages	Disadvantages	
		Electrolyte	Membrane	Temperature				
Batch	H cell	Liquid electrolyte (KHCO <sub>3</sub> , ionic liquids, etc.)	CEM, AEM, or membraneless	Range dependent on the electrolyte, membrane, and pressure chosen	<100 mA cm <sup>-2</sup>	Stability limited to stability of catalyst, simple setup	Mass transport limitations, limited electrolytes (neutral or acidic), low currents, not scalable	
Electrolyzer architecture	Liquid-phase electrolyzer (alkaline electrolyzer)	Liquid electrolyte with various pH (KHCO <sub>3</sub> , KOH, ionic liquids, etc.)	CEM, AEM, or membraneless	Range dependent on the electrolyte and pressure chosen	>1 A cm <sup>-2</sup>	Precise control of reaction environment, high current densities	Ohmic losses, flooding, complexity in system setup (pumps for electrolyte), carbonate salt formation	
	Gas-phase electrolyzer (polymer electrolyte membrane)	Cation exchange	Solid polymer (CEM)	CEM (i.e., Nafion, SPEEK, etc.)	Range dependent on the electrolyte, membrane, and pressure chosen	100 mA cm <sup>-2</sup>	Similarity to H <sub>2</sub> O electrolyzer makes scale-up easier, low ohmic losses	Competition in selectivity between HER and CO <sub>2</sub> RR, hydration of membrane, acidification of cathode
		Anion exchange	Solid polymer (AEM)	AEM (Fumasep, sulfonated PVA, AMI 7001, Sustainion, Fumatech, etc.)	Range dependent on the electrolyte, membrane, and pressure chosen	Hundreds of mA cm <sup>-2</sup>	Low ohmic losses, stability	Hydration of membrane and gas stream (catholyte-free system), carbonate ion formation
	Bipolar	Solid polymer (BPM)	BPM (AEM and CEM together, Fumasep FBM)	Range dependent on the electrolyte, membrane, and pressure chosen	200 mA cm <sup>-2</sup>	Stability, pH balance in cell, decreased liquid product loss	Hydration of membrane and gas stream, acidification of cathode, higher ohmic losses across membrane	
	Solid oxide electrolyzer	Solid oxide	None	<600 °C	>1 A cm <sup>-2</sup>	High current densities, good energy efficiencies	Mostly single-carbon products	

serves several purposes. First, it prevents CO<sub>2</sub>RR products from crossing over to the anode where they can be oxidized back into CO<sub>2</sub>. In addition, ion-exchange membranes restrict evolved O<sub>2</sub> at the anode from crossing over to the cathode and stealing electrons for ORR that could otherwise be used for CO<sub>2</sub>RR. The choice of ion-exchange membrane, cation-exchange membrane (CEM), anion-exchange membrane (AEM), or bipolar membrane (BPM) depends on the products of interest. For ionic CO<sub>2</sub>RR products, using the opposite type of ion-exchange membrane (i.e., a CEM for an anionic species, like formate) can prevent product crossover and loss.<sup>[137]</sup> Moreover, the selection of suitable membranes should also be based on the pH of the electrolytes used. For example, Dufek et al. extended the lifetime of their syngas (CO and H<sub>2</sub>) producing cell with an AEM, by maintaining a high anode pH.<sup>[138]</sup> Another approach is to remove the membrane, and rely on laminar electrolyte flow to mitigate crossover, akin to microfluidic fuel cells.<sup>[139,140]</sup> Removing the membrane reduces ohmic loss, simplifies the system requirements, decreases capital costs, and alleviates salting out issues.<sup>[141,142]</sup> However, this approach is not suitable for electrolyzers that generate liquid products while operating with recirculating electrolyte. In addition, it is difficult to maintain the laminar flow barrier when scaling these systems up in size, manifold length, and current density.

Liquid-phase electrolyzers have achieved high current densities toward CO,<sup>[143–148]</sup> formate,<sup>[149–151]</sup> and multicarbon

hydrocarbons/oxygenates.<sup>[74,126,129,152,153]</sup> With control of fluid streams on both sides of the electrode, this configuration allows for precise control and optimization of the reaction environment (electrolyte tuning is discussed in Section 5.3). While having a liquid electrolyte can be beneficial, it is also a source of instability in the system due to impurity deposition on the catalyst and the potential penetration of liquid electrolyte into the gas diffusion electrode, or flooding, which is a common failure mode. Some initial systems were designed to force gas-phase CO<sub>2</sub> through the gas diffusion electrode into the liquid channel rather than providing a gas channel exit.<sup>[138,154–158]</sup> Recently, Haas et al. generated CO at 50 mA cm<sup>-2</sup> for over 1000 h by forcing the CO<sub>2</sub> through their gas diffusion electrode; however, they did not operate at higher current densities without sacrificing selectivity.<sup>[106]</sup> In addition to increasing ohmic resistance of electrolytes through bubble production, forcing CO<sub>2</sub> in alkaline electrolytes can lead to bicarbonate/carbonate formation and salt precipitation, which reduce electrolyte conductivity, alter electrolyte pH, and block gas diffusion electrode/membrane pores. Jeanty et al. exploited minor flooding of the gas diffusion electrode to clean off salt precipitate that had accumulated over time, allowing them to produce CO for over 600 h.<sup>[159]</sup> While good selectivity and current densities have been demonstrated, further advances in gas diffusion electrode design (recent examples in Section 5.2) are needed to increase the stability of these liquid-phase electrolyzers.

### 5.1.2. Gas-Phase Electrolyzer

This class of flow cell architecture resembles PEM electrolyzers. Gas-phase electrolyzers consist of a cathode and anode separated by a solid polymer electrolyte (ion-exchange membrane). The catalyst on the cathode is directly pressed against the ion-exchange membrane in a zero-gap configuration. A key difference for gas-phase reactors is that humidity must be provided to the system, through a liquid electrolyte on the anode side and/or through humidification of the gas inlet stream, to keep the membrane hydrated during operation. Gas-phase electrolyzers have several advantages over their liquid-phase counterparts as they involve less electrolyte pumps and flow fields, can be pressurized easily, and have lower ohmic losses. Also, the elimination of catholyte removes the possibility of electrolyte flooding the gas diffusion electrode, electrolyte impurity deposition onto the catalysts, and the generation of bicarbonate/carbonate salts, thereby removing multiple sources of instability. However, liquid products can accumulate in the gas diffusion electrodes and hamper gas diffusion. Highly wetting alcohol products are particularly challenging to handle. The successful extraction of the liquid products from the gas diffusion electrodes can maintain stability and has the potential to produce a stream of concentrated liquid products.

The majority of gas-phase CO<sub>2</sub>RR studies have been conducted with CEMs. In this configuration, protons (H<sup>+</sup>) or other cations travel from the anode to the cathode through the CEM. In direct comparisons with liquid-phase electrolyzers, gas-phase CEM electrolyzers have shown improved performance attributed to improved CO<sub>2</sub> availability. For example, Lee et al. observed a significant improvement in their formate FE and stable multiday production when using a gas-phase system compared to a liquid-phase electrolyzer.<sup>[160]</sup> Researchers have also used catalysts that have poor CO<sub>2</sub>RR selectivity in liquid-phase electrolyzers (Pt, Fe, Fe–Co, Pt–Ru, etc.) to produce products not typically observed in other flow cell systems, such as methanol,<sup>[161–164]</sup> isopropanol,<sup>[165,166]</sup> and >C<sub>5</sub> long-chain products, although in small quantities.<sup>[167,168]</sup> These longer-chain products may be more readily detected in these systems owing to their increased concentrations not being diluted in a bulk liquid electrolyte, multistep upgrading made possible by catalyst-confined shorter-chain liquid products as reaction intermediates, or the enabling of distinct reaction pathways. Moreover, changes in product selectivity have been attributed to the influence of proton transport within the membrane, with poor proton transport favoring products requiring less proton transfers.<sup>[169]</sup> On the other hand, the acidification of the cathode compartment over time can be an issue in these systems, especially at higher current densities, leading to increased HER and decreased CO<sub>2</sub>RR.<sup>[170,171]</sup> Researchers have managed to circumvent this acidification by including a buffer layer between the catalyst and membrane; however, these layers may not be effective for long-run timescales, increase the resistance of the cell, and negate some of the most attractive features of gas-phase electrolyzers.<sup>[172]</sup> Controlling proton transport and the local catalyst environment is the key to higher CO<sub>2</sub>RR selectivity in these membrane systems.

In AEM gas-phase electrolyzers, hydroxides (OH<sup>−</sup>) or other anions are the charge carrier in the membrane. Unlike CEM

systems, when an AEM is used, water dissociation at the cathode provides the necessary protons for CO<sub>2</sub>RR. In this case, the humidity in the gas stream and/or membrane will act as the water source. Owing to the decreased proton availability, AEM systems typically have less competition from HER.<sup>[173]</sup> In addition, reduced proton availability in the AEM system can influence the CO<sub>2</sub>RR product distribution. For instance, Komatsu et al. reasoned that differences in proton availability led to C<sub>2</sub>H<sub>4</sub> as the major product with a CEM and HCOOH as the major product with an AEM under otherwise similar conditions.<sup>[174]</sup> Similarly, type of membrane used can also influence product selectivity.<sup>[175,176]</sup> In the absence of a liquid electrolyte stream with which to control the local reaction environment, membranes have been functionalized to tune selectivity and other performance parameters.<sup>[177]</sup> For instance, AEMs functionalized with imidazolium have been used to produce CO or syngas at moderate (50 mA cm<sup>−2</sup>) and high current densities (≥100 mA cm<sup>−2</sup>), operating with high stability for hours,<sup>[99]</sup> days,<sup>[178]</sup> and even months.<sup>[179]</sup> Further tuning of membrane properties could allow for the precise control of product selectivity and cell voltage. In contrast with liquid-phase electrolyzers, the electrolyte in gas-phase electrolyzers is a manufactured part of the cell and thus presents some unique opportunities. For instance, the solid electrolyte membrane can be designed to reflect the surrounding manifold geometries or to have properties varying in the downstream direction to reflect the changing composition of a reactant stream.

BPMs, consisting of an AEM and a CEM laminated together, are used in some water electrolyzers<sup>[180–183]</sup> and have been recently applied to CO<sub>2</sub> electrolyzers. BPMs solve the problem of pH gradient development in monopolar membrane systems, which can result in voltage fluctuations and instability over time, by maintaining a constant pH in each side of the cell.<sup>[184]</sup> For example, Li et al. demonstrated the reduction of CO<sub>2</sub> to syngas using a BPM configuration with a Bi/ionic liquid catalyst for 14 h at 80 mA cm<sup>−2</sup>.<sup>[185]</sup> Although the cell voltage was extremely stable over the run time, the FE<sub>CO</sub> decreased significantly after the first hour due to cathode acidification. Salvatore et al. improved the product selectivity of this type of system through the addition of a solid-supported aqueous NaHCO<sub>3</sub> layer between their BPM and Ag catalyst. With this modification, their system ran for over 24 h at 100 mA cm<sup>−2</sup> and 65% FE<sub>CO</sub>.<sup>[186]</sup> Moreover, unlike AEMs, BPMs inhibit the loss of the cathodic liquid products to the anode via electromigration, diffusion, and/or electroosmotic drag, resulting in higher concentrations of recovered products.<sup>[187]</sup> While gas-phase electrolyzers show promise for CO<sub>2</sub>RR, it remains a challenge to operate them at higher current densities (>200 mA cm<sup>−2</sup>) with high product selectivity, and multicarbon products remain elusive.

### 5.1.3. Solid Oxide Electrolyzer

The solid oxide flow cell architecture resembles that of solid oxide electrolyzers. This cell consists of a solid cathode, anode, and electrolyte. They utilize zirconia-based oxides, ceria-based oxides, or lanthanum gallate-based oxides as the solid electrolyte. Solid oxide electrolyzers combine electrocatalysis with

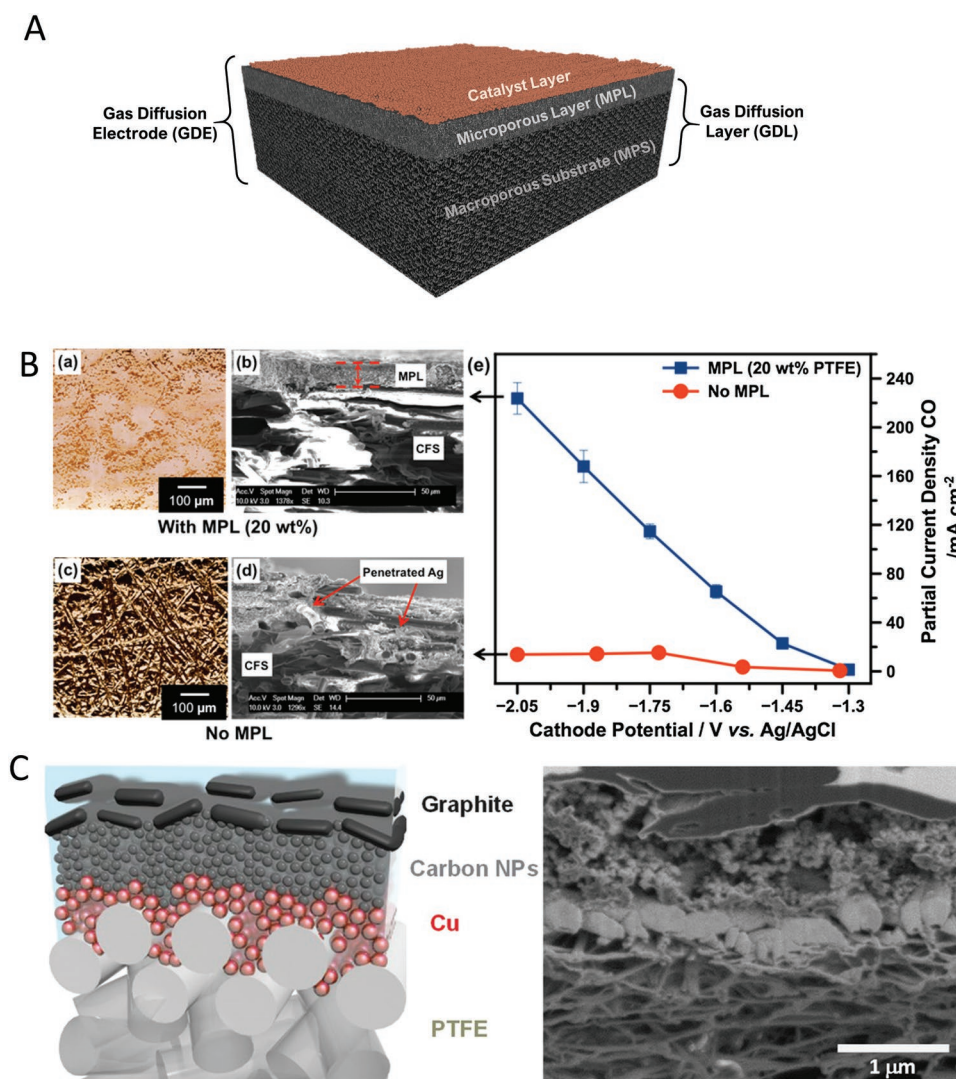


**Figure 10.** A) Structure of a conventional carbon-based gas diffusion electrode. B) Study of the effect of the microporous layer on the gas diffusion electrode performance. B) Reproduced with permission.<sup>[192]</sup> Copyright 2016, Elsevier. C) Gas diffusion electrode structure developed by Dinh et al. to operate over 150 h. Reproduced with permission.<sup>[74]</sup> Copyright 2018, AAAS.

high temperatures (>600 °C) to generate C<sub>1</sub> gas products like CO or CH<sub>4</sub>, at high current densities, typically on the order of A cm<sup>-2</sup>, from CO<sub>2</sub> and H<sub>2</sub>O/H<sub>2</sub> (proton source) feedstocks. Although this configuration operates at low cell voltages and high current densities with high stability, the extreme temperature requirement and limited product range restrict more widespread use.<sup>[188–191]</sup>

## 5.2. Gas Diffusion Electrodes

Gas diffusion electrodes (Figure 10a) are at the heart of most water electrolyzers, and are integral to both gas- and liquid-phase CO<sub>2</sub> electrolyzers. Gas diffusion electrodes are composed of a gas diffusion layer with a catalyst layer deposited on one side. Gas diffusion electrodes allow for direct gas-phase CO<sub>2</sub> delivery from a gas inlet channel to the catalyst surface through a gas diffusion layer. The gas diffusion layer is a hydrophobic,

porous, and conductive structure consisting of two layers, a microporous layer and a macroporous substrate. Most commercially available gas diffusion layers have been optimized for electrolyzer and fuel cell applications, and while they share similar functions in CO<sub>2</sub> electrolyzers, few comprehensive studies have been performed to optimize each component of the gas diffusion layer for CO<sub>2</sub>RR applications.

The macroporous substrate serves the function of providing mechanical stability and electrical contact, as well as distributing gas through its macroscale pores. Typical materials used for the macroporous substrate are carbon structures (paper, cloth, etc.).<sup>[193]</sup> Using a liquid-phase CO<sub>2</sub> electrolyzer, Kim et al. studied the effect of macroporous substrate thickness where notably higher current densities toward CO formation were achieved at a fixed cell voltage when using a thin, 60 μm substrate.<sup>[192]</sup>

The microporous layer, located between the macroporous substrate and the catalyst layer, is added to enhance interfacial



electrical connection (Figure 10b) and to prevent flooding. The microporous layer is commonly composed of a mixture of carbon black nanoparticles and a hydrophobic polymer, usually polytetrafluoroethylene (PTFE), and forms a layer with pores on the order of 200 nm.<sup>[193]</sup> To prevent flooding, especially in liquid-phase electrolyzers, the PTFE content of the microporous layer can be increased at the expense of electrical conductivity and gas permeability.<sup>[192]</sup> In liquid-phase electrolyzers, Li et al. determined that a 30% PTFE loading yielded high CO<sub>2</sub> permeability,<sup>[194]</sup> while Kim et al. obtained the highest currents for CO production using a PTFE loading of 20% at the same cell voltage.<sup>[192]</sup> Recently, Dinh et al. developed a gas diffusion layer that decoupled the hydrophobicity and electrical conductivity requirements of the microporous layer (Figure 10c), enabling 150 h of continuous operation in a highly alkaline liquid-phase electrolyzer.<sup>[74]</sup>

CO<sub>2</sub> reduction takes place at the catalyst layer in the gas diffusion electrode. Just as in water electrolyzers, catalyst layers for CO<sub>2</sub>RR are typically comprised of a mixture of catalyst nanoparticles and a binder, such as Nafion. When an ionomer like Nafion is used as a binder, it improves catalyst utilization through increased ionic connection, but it comes at the expense of elevated water content in pores owing to the hydrophilic nature of Nafion.<sup>[195]</sup> Using Sn catalysts in liquid-phase electrolyzers, one study found 20 wt% Nafion to yield the highest CO<sub>2</sub>RR partial currents, whereas another study found the highest FE<sub>HCOOH</sub> at an optimal loading of 50 wt% Nafion.<sup>[196,197]</sup> Wang et al. added 11% PTFE to their Nafion-based ink to find that their current density and product selectivity both increased by ≈25% due to the more porous catalyst layer structure improving gas diffusion and increasing surface area.<sup>[198]</sup>

Supporting carbon materials in fuel cells allow for significantly reduced catalyst loadings and improved performance.<sup>[195]</sup> Similarly, in CO<sub>2</sub>RR, Delacourt et al. found that catalysts with 20 wt% acetylene black support exhibited higher CO<sub>2</sub>RR selectivity compared to their unsupported counterparts.<sup>[172]</sup> Moreover, by replacing carbon black with TiO<sub>2</sub> as the catalyst support, both at 40 wt%, allowed Ma et al. to nearly double the CO<sub>2</sub>RR partial current at the same cell voltage.<sup>[148]</sup> In a later report, they produced a fourfold increase in partial current density of CO when integrating carbon foam as the supporting material in place of carbon black.<sup>[199]</sup>

To achieve high catalyst utilization, the catalyst particles must be connected both ionically and electrically, making catalyst deposition critical to performance. Some researchers have adhered catalyst to the gas diffusion layer via solvent-free dry pressing<sup>[137]</sup> and rolling techniques,<sup>[200]</sup> whereas others have synthesized the catalyst material directly on the gas diffusion layer via electrodeposition.<sup>[201–203]</sup> However, it is most common for a binder–catalyst mixture to be drop-cast or spray-deposited.<sup>[153,158,204,205]</sup> Comparing different deposition methods, Jhong et al. found that cathodes that were air-brushed outperformed hand-painted and screen-printed cathodes in terms of current density.<sup>[147]</sup> Moreover, physical vapor deposition methods used in the semiconductor industry, such as evaporation and sputtering as used by Dinh et al. for CO<sub>2</sub>RR,<sup>[74]</sup> are amenable to large-scale production and can controllably deposit sub-micrometer thicknesses of catalyst materials.

### 5.3. Reaction Environment Engineering

#### 5.3.1. Electrolyte Engineering

The liquid electrolyte plays an integral role in H cell and liquid-phase electrolyzers as it enables ionic transport of protons and provides the reaction environment. Although ionic liquids<sup>[206,207]</sup> and organic electrolytes<sup>[208,209]</sup> have been used, the vast majority of CO<sub>2</sub>RR studies have been performed in aqueous electrolytes. For a summary of recent advances in the other electrolyte types, the reader is directed to dedicated reviews.<sup>[210–212]</sup> In this section, we outline three major areas of study for aqueous electrolytes: pH, cation, and anion effects.

The pH of the electrolyte is central to reaction selectivity and overpotentials. There is a distinction between bulk electrolyte pH and local cathode pH, as reduction reactions drive up the local pH at the electrode surface.<sup>[213]</sup> Numerous studies have demonstrated unique pH dependencies for CO<sub>2</sub>RR products. For example, when generating CO on Ag catalysts in liquid-phase electrolyzers, alkaline conditions have resulted in reduced overpotentials<sup>[146,214]</sup> and HER<sup>[215]</sup>; however, as the pH is increased, the selectivity of CO decreases in favor of formate formation.<sup>[47,146]</sup> As for the production of formate, various studies in both H cells and flow cells have found that a bulk pH in the range of 2–4 yields the optimal selectivity with p-block metal catalysts.<sup>[140,216,217]</sup> With respect to C<sub>2</sub>H<sub>4</sub>, formation is largely independent of pH,<sup>[218]</sup> unlike the formation of CH<sub>4</sub> that is pH dependent. Thus, in H cells, solutions with weak buffering abilities have been shown to increase the ratio of C<sub>2</sub>H<sub>4</sub> to CH<sub>4</sub>.<sup>[219–221]</sup> Flow cells operating under alkaline conditions have achieved improved selectivity for C<sub>2</sub>H<sub>4</sub> at reduced overpotentials.<sup>[74,153]</sup> In general, alkaline conditions, only accessible through flow cell operation, benefit the formation of the products of interest through reduced overpotentials, reduced HER, and/or improved selectivity.

Cation effects have received a great deal of focus in the field of CO<sub>2</sub>RR, specifically the influence of alkali metals, such as Na<sup>+</sup> and K<sup>+</sup>. Studies have demonstrated that larger cations, Cs<sup>+</sup> and K<sup>+</sup>, can greatly increase the total current density,<sup>[222,223]</sup> suppress the HER,<sup>[219,224]</sup> and improve selectivity toward multicarbon products, especially C<sub>2</sub>H<sub>4</sub>.<sup>[225,226]</sup> The larger, less hydrated, cations adsorb easily on the catalyst surface making the potential at the outer Helmholtz plane more positive and thereby reducing the concentration of H<sup>+</sup> ions and impeding the formation of H<sub>2</sub> and CH<sub>4</sub>.<sup>[219,222,224,225,227]</sup> Alternatively, Singh et al. have recently claimed that larger cations provide stronger buffering abilities, maintain a lower pH, and keep the local dissolved CO<sub>2</sub> concentration higher (Figure 11). The higher CO<sub>2</sub> concentrations reduce polarization losses, which preferentially improves selectivity toward C<sub>2</sub>H<sub>4</sub> over CH<sub>4</sub> and H<sub>2</sub>.<sup>[228]</sup> Moreover, larger cation concentrations can greatly reduce charge transfer resistances by helping to stabilize the \*CO<sub>2</sub><sup>δ-</sup> anion radical and leading to higher current densities at the same applied potentials.<sup>[204,223,224]</sup>

Anion effects are less studied than cation effects. The most commonly employed anion in aqueous electrolytes is bicarbonate (HCO<sub>3</sub><sup>-</sup>), although some studies have been performed with hydroxide (OH<sup>-</sup>), sulfate, and various halides.<sup>[228,229]</sup> Verma et al. discovered that the best selectivity and lowest overpotentials for CO production were obtained in the following order:

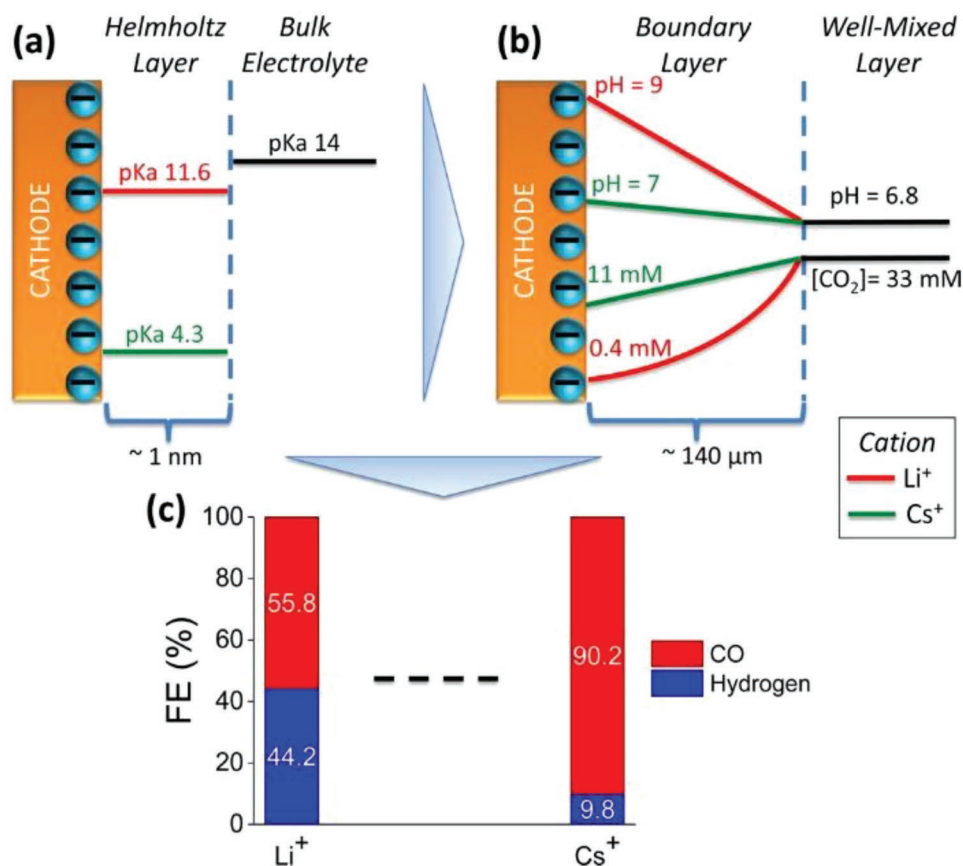


**Figure 11.** a)  $pK_a$  of hydrolysis for  $\text{Li}^+$  and  $\text{Cs}^+$  inside the Helmholtz layer and in the bulk electrolyte. b) The distribution of pH and  $\text{CO}_2$  concentration in the boundary layer. c) The improved experimental selectivity toward the  $\text{CO}_2\text{RR}$  as compared to the HER when using larger cations on a Ag catalyst. a–c) Reproduced with permission.<sup>[228]</sup> Copyright 2016, the American Chemical Society.

$\text{OH}^- > \text{HCO}_3^- > \text{Cl}^-$ .<sup>[204]</sup> They suggested that weakly solvated anions, such as  $\text{Cl}^-$ , interact directly with the electrode surface and can destabilize the  $^*\text{CO}_2^{\delta-}$  intermediate, unlike smaller, more hydrated, anions that are located further away (Figure 12). Studying the effects of different halides, Varela et al. demonstrated that while both  $\text{Cl}^-$  and  $\text{Br}^-$  can be used to suppress HER and improve the selectivity toward CO,  $\text{I}^-$  can enhance hydrocarbon formation by donating more electronic charge to the Cu surface and facilitating charge transfer.<sup>[230]</sup>

In addition to the specific anion or cation effects on reaction kinetics, the cost and conductivity of the electrolyte solution (i.e., the concentration and composition of the electrolyte solution) are important considerations when operating flow cell electrolyzers. Ohmic losses may be prohibitively large in the case of less conductive electrolytes, such as 0.1 M  $\text{KHCO}_3$  (conductivity of  $10 \text{ mS cm}^{-1}$  as compared to 1.0 M  $\text{KOH}$  that has a conductivity of  $220 \text{ mS cm}^{-1}$ ),<sup>[231,232]</sup> where the energy efficiency would be greatly impacted and more expensive electrolytes, such as  $\text{CsHCO}_3$ , may be too costly to justify large-scale implementation.

### 5.3.2. Pressure

Pressure affects both electrochemical performance and industrial integration with up- and downstream processes. There

have been relatively few systematic studies of pressurized flow cells,<sup>[146,154–156,158,233]</sup> with most pressure studies being performed in H cell reactors, and pressures in the range of 1–60 atm. The primary benefit of elevated pressure is well evidenced in H cell reactors, the enhanced  $\text{CO}_2$  solubility in aqueous electrolytes, which allows for higher  $\text{CO}_2\text{RR}$  current densities.<sup>[234,235]</sup> On the other hand, even with the mass transport benefits afforded by gas diffusion electrodes in flow cells, Dufek et al. found a fourfold improvement in  $\text{FE}_{\text{CO}}$  and a corresponding decrease in HER when operating at elevated pressures of 20 atm.<sup>[154,233]</sup>

Pressure not only influences the selectivity between  $\text{CO}_2\text{RR}$  and HER, but also modulates the selectivity between  $\text{CO}_2\text{RR}$  products and/or affects overpotentials. For catalysts producing CO (Au, Ag, etc.) or formate (Sn, Pb, etc.), elevated pressures do not greatly influence selectivity,<sup>[154,158,216,233,234,236–239]</sup> but reduce cathodic overpotentials.<sup>[146,158,234,237,238]</sup> In addition, some catalysts (Fe, Co, Rh, Ni, Pd, Pt, and C) with predominantly  $\text{H}_2$  selectivity at 1 atm can generate CO or  $\text{HCOOH}$  when pressurized.<sup>[155,156,158,236,240–242]</sup> It has been hypothesized that the high pressure of  $\text{CO}_2$  stimulates the desorption of CO molecules from the catalyst surface that are otherwise tightly bound at ambient conditions.<sup>[241,243]</sup> For Cu catalysts, increasing pressure typically results in increased CO production at the same applied potential<sup>[220,235]</sup> due to stimulated desorption of

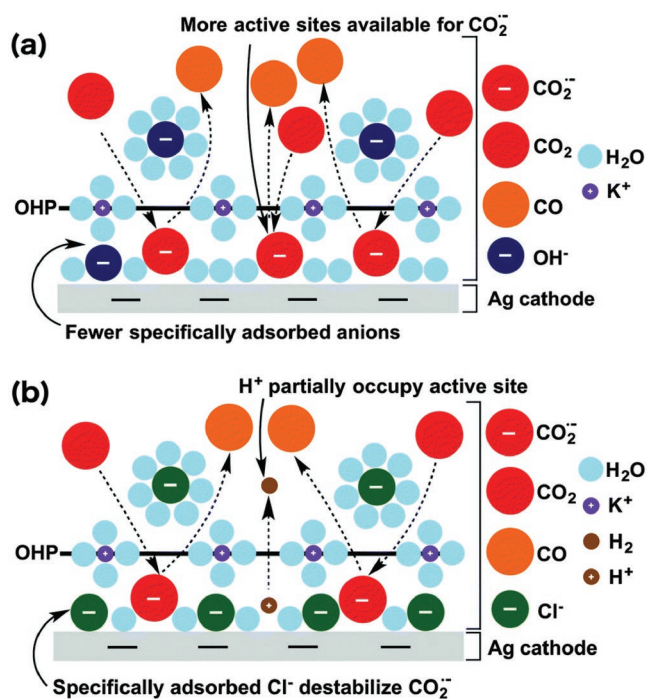


**Figure 12.** Schematic illustration demonstrating the arrangement of the electrode for a) more hydrated anions such as  $\text{OH}^-$  and b) less hydrated anions such as  $\text{Cl}^-$ . a,b) Reproduced with permission.<sup>[204]</sup> Copyright 2016, the Royal Society of Chemistry.

intermediates from the surface.<sup>[244,245]</sup> To produce hydrocarbons on pressurized Cu, the current density must be increased.<sup>[220,235]</sup> In addition to minimizing HER, tuning selectivity, and/or minimizing overpotentials, pressurization can reduce bubble size in the liquid electrolyte when operating at high current densities, minimizing the bubble-induced blockages of electrode active area and ohmic losses.

### 5.3.3. Temperature

In commercial alkaline and PEM water electrolyzers, low-temperature systems are operated at temperatures of at least 60 °C.<sup>[246]</sup> Heating can be applied externally, or generated internally as a product of reactions and ohmic losses.<sup>[157,247]</sup> The role of temperature in  $\text{CO}_2\text{RR}$  electrolyzer performance is complex as many properties of the reactor, reactants, and reaction kinetics exhibit unique sensitivities to temperature (Figure 13).

Most temperature studies performed to date have been conducted in H cell reactors where the  $\text{CO}_2$  solubility determines the attainable partial current for  $\text{CO}_2\text{RR}$ . In these systems, the increased  $\text{CO}_2$  solubility achieved at lower temperatures (Figure 13) improves the selectivity for  $\text{CO}_2\text{RR}$  as compared to HER.<sup>[251–256]</sup> While the dominant products of  $\text{CO}_2\text{RR}$  do not change

significantly with temperature on most catalysts,<sup>[252]</sup> studies on Cu have demonstrated that hydrocarbon selectivity tends to shift from  $\text{CH}_4$  to  $\text{C}_2\text{H}_4$  as temperature increases.<sup>[254,257–259]</sup> This improved  $\text{C}_2\text{H}_4$  selectivity is attributed to reduced activation energies<sup>[252]</sup> and enhanced surface diffusion of adsorbed intermediates.<sup>[254]</sup>

To mitigate temperature-induced  $\text{CO}_2$  concentration effects, researchers have pressurized systems to study other impacts of temperature. On pressurized Ni and Fe, the selectivity toward longer-chain hydrocarbon products increased with temperature up to 80 °C.<sup>[241,260]</sup> Moreover, Pb operating at a constant pressure and temperatures of 60–80 °C yielded significant increases in both current density and formate selectivity.<sup>[238,261]</sup> Therefore, when the  $\text{CO}_2$  concentration is high enough in H cells to negate the decrease in solubility of the  $\text{CO}_2$ , increasing the temperature can have net positive effects on product selectivity and current density.

There are only a few published systematic temperature studies using liquid-phase electrolyzers.<sup>[156,157]</sup> Here, the most comprehensive example is that of Dufek et al. who demonstrated an 18% improvement in their EE by increasing the temperature of their flow cell from 18 to 70 °C.<sup>[157]</sup> By comparison, there are many examples of gas-phase electrolyzers operated at temperatures in the range of 60–80 °C.<sup>[164,168,178,205]</sup> Here, the reduced  $\text{CO}_2$  solubility is less concerning and the elevated temperatures offer improved electrochemical kinetics and increased humidity content (Figure 13). For example, Lee et al. found that elevating the operating temperature from 30 to 70 °C doubled their  $\text{CO}_2\text{RR}$  partial current density at the same cell voltage.<sup>[160]</sup> The maximum operating temperature of the membrane is typically 90 °C and should not be exceeded so as to avoid reduced proton mobility through the membrane,<sup>[169]</sup> as well as flooding due to increased water crossover from the anode.<sup>[160,262]</sup> Recent advances in membrane technology have allowed higher temperatures to be used during cell operation. Notably, a recent

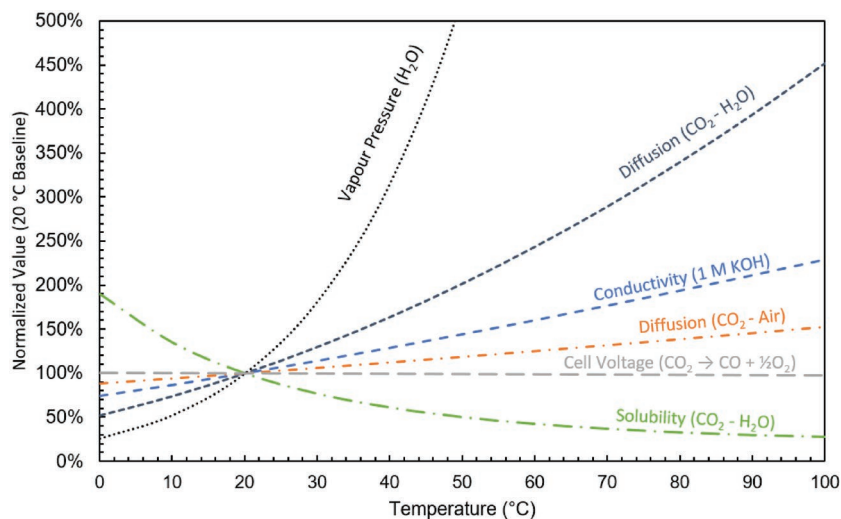


**Figure 13.** Variation of different parameters with temperature as normalized to 20 °C baseline: vapor pressure of water,<sup>[248]</sup> diffusion of  $\text{CO}_2$  in water (predicted by the Stokes–Einstein equation using the viscosity of water),<sup>[249]</sup> specific conductivity of 1 M KOH,<sup>[231]</sup> diffusion of  $\text{CO}_2$  in air,<sup>[250]</sup> cell voltage for a  $\text{CO}_2$  to CO electrolyzer with the OER on the anode side (tabulated using thermodynamic values from ref. [248]), and  $\text{CO}_2$  solubility in water.<sup>[136]</sup>

work by Gutiérrez-Guerra et al. employed a  $\text{H}_3\text{PO}_4$ -doped polybenzimidazole-polymer electrolyte membrane, which enabled electrolyzer operation at  $110^\circ\text{C}$ .<sup>[263]</sup> Elevated temperatures offer promising routes to increase conductivity and improve reaction kinetics. Reduced  $\text{CO}_2$  solubility and evaporation are challenges at elevated temperatures, but pressurization and gas-phase electrolyzers can overcome these issues.

In summary, flow cell systems are becoming the standard platform for  $\text{CO}_2\text{RR}$  development and testing. Gas- and liquid-phase electrolyzers, and the materials and fluid streams within, present vast opportunities for customization and optimization. While most developments in the field to date can be categorized as either catalyst or system contributions, many of the coming breakthroughs will be integrated, coordinated efforts with bespoke system architectures that realize and demonstrate material innovation.

## 6. Conclusions

We have summarized recent research and development progress in electrochemical  $\text{CO}_2\text{RR}$ . Great strides have been made toward bringing this technology closer to industrial relevance. Several challenges remain on the path to achieve performance targets for economically viable products.

The TEA reveals that the most economically compelling target products include  $\text{CO}$ ,  $\text{HCOOH}$ ,  $\text{C}_2\text{H}_4$ , and  $\text{C}_2\text{H}_5\text{OH}$ . The TEA also showed the key performance targets are FE (90%), cell voltage ( $<1.8\text{ V}$ ), current density ( $>300\text{ mA cm}^{-2}$ ), and stability ( $>80\,000\text{ h}$ ). Nonetheless, a detailed analysis of  $\text{CO}_2$  electrolyzer cost is needed to build an accurate techno-economic model for  $\text{CO}_2\text{RR}$  technology.

While high FEs toward  $\text{CO}$ ,  $\text{HCOOH}$ , and  $\text{C}_2\text{H}_4$  ( $\approx 70\%$ ) have been demonstrated, high selectivity toward  $\text{C}_2\text{H}_5\text{OH}$  is yet to be achieved. Several promising strategies to further enhance the selectivity include, but are not limited to, nanostructuring the catalyst material, alloying, inducing surface strain, functionalizing the catalyst surface, or tuning the chemical environment. In addition, the ultimate commercial viability of these strategies will require catalyst synthesis routes that are scalable.<sup>[71]</sup>

Advances in the mechanistic understanding of  $\text{CO}_2\text{RR}$  are also needed to move away from the current trial-and-error paradigm and toward accelerated, rational design of catalyst materials. Accurate DFT models that include the realities of surface coverage, electrolyte properties, and electric field influence are essential for a deeper, more reliable picture of reaction mechanisms. Accurate DFT modeling will further feed and enable high-throughput machine learning guided calculations and process optimization. Once sufficient quantity and quality of foundational data for machine learning models is available, the field can better navigate the vast parameter space of chemical, material, and mechanical variables inherent to the  $\text{CO}_2\text{RR}$  challenge.

By departing from traditional H cell configurations and the implementing liquid/gas-phase electrolyzers, a number of groups have demonstrated high current density ( $>100\text{ mA cm}^{-2}$ )  $\text{CO}_2$  conversion—a necessary condition for industrial applicability. A remaining barrier to commercialization of this technology is the stability of the catalyst and/or the electrodes in

these systems. Therefore, significant research efforts toward understanding the failure mechanisms and improving the lifetime of  $\text{CO}_2\text{RR}$  cathodes will be crucial going forward.

Given the dominance of electrical energy input cost on the techno-economic potential of  $\text{CO}_2\text{RR}$ , energy efficiency is of particular importance for the field. However, full cell EE performances are rarely reported while component metrics such as FE are emphasized. In many cases, high FEs for products of interest have been achieved with high overpotentials that are detrimental to the overall EE and the ultimate applicability. Significant reductions in cell resistance and overpotential for both  $\text{CO}_2\text{RR}$  and the corresponding anode reaction, typically OER, are necessary as the field and technology mature. In addition,  $\text{CO}_2\text{RR}$  is often performed in a different environment than the optimal OER conditions, introducing increased membrane resistances or other full cell kinetic and polarization losses, which are not typically captured in reported metrics. Full cell metrics and economics will be improved by exploring alternative anodic reactions that generate a valued product<sup>[264]</sup> and/or reduce the required potential. In summary,  $\text{CO}_2$  electrolyzer performance must be assessed on full cell figure of merit: this will provide the needed baseline for comparison, and will inspire and guide the development and optimization of  $\text{CO}_2\text{RR}$  viable at scale for both commercial and environmental benefit.

## Acknowledgements

All authors contributed equally to this work. This work was financially supported by the Ontario Research Fund: Research Excellence Program, the Natural Sciences and Engineering Research Council (NSERC) of Canada, and the CIFAR. A.S. wishes to thank Fonds de Recherche en Nature et Technologies for support in the form of postdoctoral fellowship award. D.S. acknowledges the NSERC E.W.R. Steacie Memorial Fellowship. M.G.K. acknowledges Banting postdoctoral fellowship from Government of Canada. C.M.G. acknowledges funding from NSERC in the form of a postdoctoral fellowship. J.P.E. thanks NSERC, Hatch, and the Government of Ontario for their support through graduate scholarships. This research was also supported by Canada Research Chairs program.

## Conflict of Interest

The authors declare no conflict of interest.

## Keywords

carbon dioxide reduction, catalytic mechanisms, electrocatalysis, electrolyzers, nanomaterials

Received: November 6, 2018

Revised: December 16, 2018

Published online:

[1] E. Kintisch, *Science* **2015**, *350*, 1018.

[2] J. Rogelj, M. den Elzen, N. Höhne, T. Fransen, H. Fekete, H. Winkler, R. Schaeffer, F. Sha, K. Riahi, M. Meinshausen, *Nature* **2016**, *534*, 631.

[3] A. A. Fawcett, G. C. Iyer, L. E. Clarke, J. A. Edmonds, N. E. Hultman, H. C. McJeon, J. Rogelj, R. Schuler, J. Alsalam,



- G. R. Asrar, J. Creason, M. Jeong, J. McFarland, A. Mundra, W. Shi, *Science* **2015**, 350, 1168.
- [4] IPCC, *Climate Change 2014: Synthesis Report. Contribution of Working Groups I, II, and III to the Fifth Assessment Report of the Intergovernmental Panel on Climate Change*, IPCC, Geneva, Switzerland **2015**.
- [5] United Nations Framework Convention on Climate Change (UNFCCC), *The Paris Agreement*, UN, Paris, France **2015**.
- [6] J. Rogelj, G. Luderer, R. C. Pietzcker, E. Kriegler, M. Schaeffer, V. Krey, K. Riahi, *Nat. Clim. Change* **2015**, 5, 519.
- [7] S. Fuss, J. G. Canadell, G. P. Peters, M. Tavoni, R. M. Andrew, P. Ciais, R. B. Jackson, C. D. Jones, F. Kraxner, N. Nakicenovic, C. Le Quéré, M. R. Raupach, A. Sharifi, P. Smith, Y. Yamagata, *Nat. Clim. Change* **2014**, 4, 850.
- [8] B. Kumar, J. P. Brian, V. Atla, S. Kumari, K. A. Bertram, R. T. White, J. M. Spurgeon, *Catal. Today* **2016**, 270, 19.
- [9] B. Endródi, G. Bencsik, F. Darvas, R. Jones, K. Rajeshwar, C. Janáky, *Prog. Energy Combust. Sci.* **2017**, 62, 133.
- [10] C. J. Barnhart, M. Dale, A. R. Brandt, S. M. Benson, *Energy Environ. Sci.* **2013**, 6, 2804.
- [11] J. P. Barton, D. G. Infield, *IEEE Trans. Energy Convers.* **2004**, 19, 441.
- [12] A. S. Brouwer, M. van den Broek, A. Seebregts, A. Faaij, *Renewable Sustainable Energy Rev.* **2014**, 33, 443.
- [13] F. H. Saadi, N. S. Lewis, E. W. McFarland, *Energy Environ. Sci.* **2018**, 11, 469.
- [14] F. Cherubini, *Energy Convers. Manage.* **2010**, 51, 1412.
- [15] G. A. Olah, A. Goepfert, G. K. S. Prakash, *J. Org. Chem.* **2009**, 74, 487.
- [16] Á. Martín, A. Navarrete, M. D. Bermejo, *J. Supercrit. Fluids* **2018**, 134, 141.
- [17] O. S. Bushuyev, P. De Luna, C. T. Dinh, L. Tao, G. Saur, J. van de Lagemaat, S. O. Kelley, E. H. Sargent, *Joule* **2018**, 2, 825.
- [18] M. Jouny, W. Luc, F. Jiao, *Ind. Eng. Chem. Res.* **2018**, 57, 2165.
- [19] S. Verma, B. Kim, H.-R. Molly Jhong, S. Ma, P. J. A. Kenis, *ChemSusChem* **2016**, 9, 1972.
- [20] P. J. G. Pearson, T. J. Foxon, *Energy Policy* **2012**, 50, 117.
- [21] R. Fouquet, P. J. G. Pearson, *Energy Policy* **2012**, 50, 1.
- [22] F. Kern, A. Smith, *Energy Policy* **2008**, 36, 4093.
- [23] F. Barbir, *Energy* **2009**, 34, 308.
- [24] K. P. Kuhl, E. R. Cave, D. N. Abram, T. F. Jaramillo, *Energy Environ. Sci.* **2012**, 5, 7050.
- [25] H. M. Torres Galvis, K. P. de Jong, *ACS Catal.* **2013**, 3, 2130.
- [26] J. M. Spurgeon, B. Kumar, *Energy Environ. Sci.* **2018**, 11, 1536.
- [27] X. Li, P. Anderson, H.-R. M. Jhong, M. Paster, J. F. Stubbins, P. J. A. Kenis, *Energy Fuels* **2016**, 30, 5980.
- [28] DOE, <https://www.energy.gov/eere/solar/sunshot-2030> (accessed: October 2018).
- [29] A. Raksajati, M. T. Ho, D. E. Wiley, *Ind. Eng. Chem. Res.* **2013**, 52, 16887.
- [30] J. B. Greenblatt, D. J. Miller, J. W. Ager, F. A. Houle, I. D. Sharp, *Joule* **2018**, 2, 381.
- [31] M. Karamad, V. Tripkovic, J. Rossmeisl, *ACS Catal.* **2014**, 4, 2268.
- [32] A. A. Peterson, F. Abild-Pedersen, F. Studt, J. Rossmeisl, J. K. Nørskov, *Energy Environ. Sci.* **2010**, 3, 1311.
- [33] R. B. Sandberg, J. H. Montoya, K. Chan, J. K. Nørskov, *Surf. Sci.* **2016**, 654, 56.
- [34] J. D. Goodpaster, A. T. Bell, M. Head-Gordon, *J. Phys. Chem. Lett.* **2016**, 7, 1471.
- [35] K. Letchworth-Weaver, T. A. Arias, *Phys. Rev. B* **2012**, 86, 75140.
- [36] S. N. Steinmann, P. Sautet, *J. Phys. Chem. C* **2016**, 120, 5619.
- [37] K. Mathew, R. Sundararaman, K. Letchworth-Weaver, T. A. Arias, R. G. Hennig, *J. Chem. Phys.* **2014**, 140, 084106.
- [38] T. Cheng, H. Xiao, W. A. Goddard, *J. Am. Chem. Soc.* **2016**, 138, 13802.
- [39] J. K. Nørskov, J. Rossmeisl, A. Logadottir, L. Lindqvist, J. R. Kitchin, T. Bligaard, H. Jónsson, *J. Phys. Chem. B* **2004**, 108, 17886.
- [40] K. Chan, J. K. Nørskov, *J. Phys. Chem. Lett.* **2015**, 6, 2663.
- [41] T. Cheng, H. Xiao, W. A. Goddard, *Proc. Natl. Acad. Sci. USA* **2017**, 114, 1795.
- [42] J. H. Montoya, C. Shi, K. Chan, J. K. Nørskov, *J. Phys. Chem. Lett.* **2015**, 6, 2032.
- [43] H. Xiao, T. Cheng, W. A. Goddard, R. Sundararaman, *J. Am. Chem. Soc.* **2016**, 138, 483.
- [44] J. Rossmeisl, E. Skúlason, M. E. Björketun, V. Tripkovic, J. K. Nørskov, *Chem. Phys. Lett.* **2008**, 466, 68.
- [45] X. Nie, M. R. Esopi, M. J. Janik, A. Asthagiri, *Angew. Chem., Int. Ed.* **2013**, 52, 2459.
- [46] X. Nie, W. Luo, M. J. Janik, A. Asthagiri, *J. Catal.* **2014**, 312, 108.
- [47] A. Seifitokaldani, C. M. Gabardo, T. Burdyny, C.-T. Dinh, J. P. Edwards, M. G. Kibria, O. S. Bushuyev, S. O. Kelley, D. Sinton, E. H. Sargent, *J. Am. Chem. Soc.* **2018**, 140, 3833.
- [48] Y. Hori, A. Murata, R. Takahashi, *J. Chem. Soc., Faraday Trans. 1* **1989**, 85, 2309.
- [49] Y. Hori, A. Murata, R. Takahashi, S. Suzuki, *J. Am. Chem. Soc.* **1987**, 109, 5022.
- [50] W. J. Durand, A. A. Peterson, F. Studt, F. Abild-Pedersen, J. K. Nørskov, *Surf. Sci.* **2011**, 605, 1354.
- [51] J. H. Montoya, A. A. Peterson, J. K. Nørskov, *ChemCatChem* **2013**, 5, 737.
- [52] K. J. P. Schouten, Z. Qin, E. Pérez Gallent, M. T. M. Koper, *J. Am. Chem. Soc.* **2012**, 134, 9864.
- [53] K. J. P. Schouten, Y. Kwon, C. J. M. van der Ham, Z. Qin, M. T. M. Koper, *Chem. Sci.* **2011**, 2, 1902.
- [54] F. S. Roberts, K. P. Kuhl, A. Nilsson, *Angew. Chem.* **2015**, 127, 5268.
- [55] F. Calle-Vallejo, M. T. M. Koper, *Angew. Chem., Int. Ed.* **2013**, 52, 7282.
- [56] H. Xiao, T. Cheng, W. A. Goddard, *J. Am. Chem. Soc.* **2017**, 139, 130.
- [57] Y. Lum, T. Cheng, W. A. Goddard, J. W. Ager, *J. Am. Chem. Soc.* **2018**, 140, 9337.
- [58] C. Shi, H. A. Hansen, A. C. Lausche, J. K. Nørskov, *Phys. Chem. Chem. Phys.* **2014**, 16, 4720.
- [59] T.-T. Zhuang, Z.-Q. Liang, A. Seifitokaldani, Y. Li, P. De Luna, T. Burdyny, F. Che, F. Meng, Y. Min, R. Quintero-Bermudez, C. T. Dinh, Y. Pang, M. Zhong, B. Zhang, J. Li, P.-N. Chen, X.-L. Zheng, H. Liang, W.-N. Ge, B.-J. Ye, D. Sinton, S.-H. Yu, E. H. Sargent, *Nat. Catal.* **2018**, 1, 421.
- [60] L. A. Kibler, A. M. El-Aziz, D. M. Kolb, *J. Mol. Catal. A: Chem.* **2003**, 199, 57.
- [61] M. Mavrikakis, B. Hammer, J. K. Nørskov, *Phys. Rev. Lett.* **1998**, 81, 2819.
- [62] Z. Chen, X. Zhang, G. Lu, *Chem. Sci.* **2015**, 6, 6829.
- [63] Z.-Q. Liang, T.-T. Zhuang, A. Seifitokaldani, J. Li, C.-W. Huang, C.-S. Tan, Y. Li, P. De Luna, C. T. Dinh, Y. Hu, Q. Xiao, P.-L. Hsieh, Y. Wang, F. Li, R. Quintero-Bermudez, Y. Zhou, P. Chen, Y. Pang, S.-C. Lo, L.-J. Chen, H. Tan, Z. Xu, S. Zhao, D. Sinton, E. H. Sargent, *Nat. Commun.* **2018**, 9, 3828.
- [64] A. A. Peterson, J. K. Nørskov, *J. Phys. Chem. Lett.* **2012**, 3, 251.
- [65] H.-K. Lim, H. Shin, W. A. Goddard, Y. J. Hwang, B. K. Min, H. Kim, *J. Am. Chem. Soc.* **2014**, 136, 11355.
- [66] Z. W. Ulissi, A. J. Medford, T. Bligaard, J. K. Nørskov, *Nat. Commun.* **2017**, 8, 14621.
- [67] Z. W. Ulissi, M. T. Tang, J. Xiao, X. Liu, D. A. Torelli, M. Karamad, K. Cummins, C. Hahn, N. S. Lewis, T. F. Jaramillo, K. Chan, J. K. Nørskov, *ACS Catal.* **2017**, 7, 6600.
- [68] K. Tran, Z. W. Ulissi, *Nat. Catal.* **2018**, 1, 696.
- [69] L. D. Chen, M. Urushihara, K. Chan, J. K. Nørskov, *ACS Catal.* **2016**, 6, 7133.
- [70] X. Duan, J. Xu, Z. Wei, J. Ma, S. Guo, S. Wang, H. Liu, S. Dou, *Adv. Mater.* **2017**, 29, 1701784.
- [71] G. O. Larrazábal, A. J. Martín, J. Pérez-Ramírez, *J. Phys. Chem. Lett.* **2017**, 8, 3933.

- [72] L. Zhang, Z.-J. Zhao, J. Gong, *Angew. Chem., Int. Ed.* **2017**, *56*, 11326.
- [73] D. D. Zhu, J. L. Liu, S. Z. Qiao, *Adv. Mater.* **2016**, *28*, 3423.
- [74] C.-T. Dinh, T. Burdyny, G. Kibria, A. Seifitokaldani, C. M. Gabardo, F. P. G. de Arquer, A. Kiani, J. P. Edwards, P. De Luna, O. S. Bushuyev, C. Zou, R. Quintero-Bermudez, Y. Pang, D. Sinton, E. H. Sargent, *Science* **2018**, *360*, 783.
- [75] F. P. García de Arquer, O. S. Bushuyev, P. Luna, C.-T. Dinh, A. Seifitokaldani, M. I. Saidaminov, C.-S. Tan, L. N. Quan, A. Propp, M. G. Kibria, S. O. Kelley, D. Sinton, E. H. Sargent, *Adv. Mater.* **2018**, *30*, 1802858.
- [76] M. Liu, Y. Pang, B. Zhang, P. De Luna, O. Voznyy, J. Xu, X. Zheng, C. T. Dinh, F. Fan, C. Cao, F. P. G. de Arquer, T. S. Safaei, A. Mephram, A. Klinkova, E. Kumacheva, T. Filleter, D. Sinton, S. O. Kelley, E. H. Sargent, *Nature* **2016**, *537*, 382.
- [77] X. Zheng, P. De Luna, F. P. García de Arquer, B. Zhang, N. Becknell, M. B. Ross, Y. Li, M. N. Banis, Y. Li, M. Liu, O. Voznyy, C. T. Dinh, T. Zhuang, P. Stadler, Y. Cui, X. Du, P. Yang, E. H. Sargent, *Joule* **2017**, *1*, 794.
- [78] S. Gao, Y. Lin, X. Jiao, Y. Sun, Q. Luo, W. Zhang, D. Li, J. Yang, Y. Xie, *Nature* **2016**, *529*, 68.
- [79] X. Min, M. W. Kanan, *J. Am. Chem. Soc.* **2015**, *137*, 4701.
- [80] A. Klinkova, P. De Luna, C.-T. Dinh, O. Voznyy, E. M. Larin, E. Kumacheva, E. H. Sargent, *ACS Catal.* **2016**, *6*, 8115.
- [81] K. Natsui, H. Iwakawa, N. Ikemiya, K. Nakata, Y. Einaga, *Angew. Chem., Int. Ed.* **2018**, *57*, 2639.
- [82] K. P. Kuhl, T. Hatsukade, E. R. Cave, D. N. Abram, J. Kibsgaard, T. F. Jaramillo, *J. Am. Chem. Soc.* **2014**, *136*, 14107.
- [83] M. Ma, B. J. Trzeźniowski, J. Xie, W. A. Smith, *Angew. Chem., Int. Ed.* **2016**, *55*, 9748.
- [84] Y. Chen, C. W. Li, M. W. Kanan, *J. Am. Chem. Soc.* **2012**, *134*, 19969.
- [85] X. Feng, K. Jiang, S. Fan, M. W. Kanan, *J. Am. Chem. Soc.* **2015**, *137*, 4606.
- [86] R. G. Mariano, K. McKelvey, H. S. White, M. W. Kanan, *Science* **2017**, *358*, 1187.
- [87] T. Cheng, Y. Huang, H. Xiao, W. A. Goddard, *J. Phys. Chem. Lett.* **2017**, *8*, 3317.
- [88] K.-S. Kim, W. J. Kim, H.-K. Lim, E. K. Lee, H. Kim, *ACS Catal.* **2016**, *6*, 4443.
- [89] Y.-C. Hsieh, S. D. Senanayake, Y. Zhang, W. Xu, D. E. Polyansky, *ACS Catal.* **2015**, *5*, 5349.
- [90] M. Cho, J. T. Song, S. Back, Y. Jung, J. Oh, *ACS Catal.* **2018**, *8*, 1178.
- [91] S. Hong, S. Lee, S. Kim, J. K. Lee, J. Lee, *Catal. Today* **2017**, *295*, 82.
- [92] C. Kim, T. Eom, M. S. Jee, H. Jung, H. Kim, B. K. Min, Y. J. Hwang, *ACS Catal.* **2017**, *7*, 779.
- [93] B. Qiao, A. Wang, X. Yang, L. F. Allard, Z. Jiang, Y. Cui, J. Liu, J. Li, T. Zhang, *Nat. Chem.* **2011**, *3*, 634.
- [94] J. Liu, *ACS Catal.* **2017**, *7*, 34.
- [95] S. Back, J. Lim, N.-Y. Kim, Y.-H. Kim, Y. Jung, *Chem. Sci.* **2017**, *8*, 1090.
- [96] T. Zheng, K. Jiang, N. Ta, Y. Hu, J. Zeng, J. Liu, H. Wang, *Joule* **2018**, *3*, 265.
- [97] H. Bin Yang, S.-F. Hung, S. Liu, K. Yuan, S. Miao, L. Zhang, X. Huang, H.-Y. Wang, W. Cai, R. Chen, J. Gao, X. Yang, W. Chen, Y. Huang, H. M. Chen, C. M. Li, T. Zhang, B. Liu, *Nat. Energy* **2018**, *3*, 140.
- [98] C. Zhao, X. Dai, T. Yao, W. Chen, X. Wang, J. Wang, J. Yang, S. Wei, Y. Wu, Y. Li, *J. Am. Chem. Soc.* **2017**, *139*, 8078.
- [99] K. Jiang, S. Siahrostami, T. Zheng, Y. Hu, S. Hwang, E. Stavitski, Y. Peng, J. Dynes, M. Gangisetty, D. Su, K. Attenkofer, H. Wang, *Energy Environ. Sci.* **2018**, *11*, 893.
- [100] K. Jiang, S. Siahrostami, A. J. Akey, Y. Li, Z. Lu, J. Lattimer, Y. Hu, C. Stokes, M. Gangishetty, G. Chen, Y. Zhou, W. Hill, W.-B. Cai, D. Bell, K. Chan, J. K. Nørskov, Y. Cui, H. Wang, *Chem* **2017**, *3*, 950.
- [101] J. Wu, R. M. Yadav, M. Liu, P. P. Sharma, C. S. Tiwary, L. Ma, X. Zou, X.-D. Zhou, B. I. Jakobson, J. Lou, P. M. Ajayan, *ACS Nano* **2015**, *9*, 5364.
- [102] P. P. Sharma, J. Wu, R. M. Yadav, M. Liu, C. J. Wright, C. S. Tiwary, B. I. Jakobson, J. Lou, P. M. Ajayan, X.-D. Zhou, *Angew. Chem., Int. Ed.* **2015**, *54*, 13701.
- [103] J. Wu, M. Liu, P. P. Sharma, R. M. Yadav, L. Ma, Y. Yang, X. Zou, X.-D. Zhou, R. Vajtai, B. I. Jakobson, J. Lou, P. M. Ajayan, *Nano Lett.* **2016**, *16*, 466.
- [104] C. W. Li, M. W. Kanan, *J. Am. Chem. Soc.* **2012**, *134*, 7231.
- [105] C. W. Li, J. Ciston, M. W. Kanan, *Nature* **2014**, *508*, 504.
- [106] T. Haas, R. Krause, R. Weber, M. Demler, G. Schmid, *Nat. Catal.* **2018**, *1*, 32.
- [107] D. Raciti, K. J. Livi, C. Wang, *Nano Lett.* **2015**, *15*, 6829.
- [108] L. Cao, D. Raciti, C. Li, K. J. T. Livi, P. F. Rottmann, K. J. Hemker, T. Mueller, C. Wang, *ACS Catal.* **2017**, *7*, 8578.
- [109] M. G. Kibria, C.-T. Dinh, A. Seifitokaldani, P. De Luna, T. Burdyny, R. Quintero-Bermudez, M. B. Ross, O. S. Bushuyev, F. P. García de Arquer, P. Yang, D. Sinton, E. H. Sargent, *Adv. Mater.* **2018**, *30*, 1804867.
- [110] A. D. Handoko, K. W. Chan, B. S. Yeo, *ACS Energy Lett.* **2017**, *2*, 2103.
- [111] X. Feng, K. Jiang, S. Fan, M. W. Kanan, *ACS Cent. Sci.* **2016**, *2*, 169.
- [112] D. Raciti, L. Cao, K. J. T. Livi, P. F. Rottmann, X. Tang, C. Li, Z. Hicks, K. H. Bowen, K. J. Hemker, T. Mueller, C. Wang, *ACS Catal.* **2017**, *7*, 4467.
- [113] A. Verdager-Casadevall, C. W. Li, T. P. Johansson, S. B. Scott, J. T. McKeown, M. Kumar, I. E. L. Stephens, M. W. Kanan, I. Chorkendorff, *J. Am. Chem. Soc.* **2015**, *137*, 9808.
- [114] Y. Lum, J. W. Ager, *Nat. Catal.* **2019**, *2*, 86.
- [115] S. Lee, D. Kim, J. Lee, *Angew. Chem., Int. Ed.* **2015**, *54*, 14701.
- [116] H. Mistry, A. S. Varela, C. S. Bonifacio, I. Zegkinoglou, I. Sinev, Y.-W. Choi, K. Kisslinger, E. A. Stach, J. C. Yang, P. Strasser, B. R. Cuenya, *Nat. Commun.* **2016**, *7*, 12123.
- [117] P. De Luna, R. Quintero-Bermudez, C.-T. Dinh, M. B. Ross, O. S. Bushuyev, P. Todorović, T. Regier, S. O. Kelley, P. Yang, E. H. Sargent, *Nat. Catal.* **2018**, *1*, 103.
- [118] D. Ren, Y. Deng, A. D. Handoko, C. S. Chen, S. Malkhandi, B. S. Yeo, *ACS Catal.* **2015**, *5*, 2814.
- [119] L. Mandal, K. R. Yang, M. R. Motapothula, D. Ren, P. Lobaccaro, A. Patra, M. Sherburne, V. S. Batista, B. S. Yeo, J. W. Ager, J. Martin, T. Venkatesan, *ACS Appl. Mater. Interfaces* **2018**, *10*, 8574.
- [120] Y. Lum, J. W. Ager, *Angew. Chem., Int. Ed.* **2018**, *57*, 551.
- [121] A. Eilert, F. Cavalca, F. S. Roberts, J. Osterwalder, C. Liu, M. Favaro, E. J. Crumlin, H. Ogasawara, D. Friebe, L. G. M. Pettersson, A. Nilsson, *J. Phys. Chem. Lett.* **2017**, *8*, 285.
- [122] C. Liu, M. P. Lourenço, S. Hedström, F. Cavalca, O. Diaz-Morales, H. A. Duarte, A. Nilsson, L. G. M. Pettersson, *J. Phys. Chem. C* **2017**, *121*, 25010.
- [123] F. Cavalca, R. Ferragut, S. Aghion, A. Eilert, O. Diaz-Morales, C. Liu, A. L. Koh, T. W. Hansen, L. G. M. Pettersson, A. Nilsson, *J. Phys. Chem. C* **2017**, *121*, 25003.
- [124] A. J. Garza, A. T. Bell, M. Head-Gordon, *J. Phys. Chem. Lett.* **2018**, *9*, 601.
- [125] M. Fields, X. Hong, J. K. Nørskov, K. Chan, *J. Phys. Chem. C* **2018**, *122*, 16209.
- [126] T. T. H. Hoang, S. Verma, S. Ma, T. T. Fister, J. Timoshenko, A. I. Frenkel, P. J. A. Kenis, A. A. Gewirth, *J. Am. Chem. Soc.* **2018**, *140*, 5791.
- [127] S. Lee, G. Park, J. Lee, *ACS Catal.* **2017**, *7*, 8594.
- [128] D. Ren, B. S.-H. Ang, B. S. Yeo, *ACS Catal.* **2016**, *6*, 8239.
- [129] S. Ma, M. Sadakiyo, M. Heim, R. Luo, R. T. Haasch, J. I. Gold, M. Yamauchi, P. J. A. Kenis, *J. Am. Chem. Soc.* **2017**, *139*, 47.
- [130] Z. Xu, E. Lai, Y. Shao-Horn, K. Hamad-Schifferli, *Chem. Commun.* **2012**, *48*, 5626.
- [131] F. Jia, X. Yu, L. Zhang, *J. Power Sources* **2014**, *252*, 85.
- [132] D. Kim, J. Resasco, Y. Yu, A. M. Asiri, P. Yang, *Nat. Commun.* **2014**, *5*, 4948.

- [133] J. Wu, S. Ma, J. Sun, J. I. Gold, C. Tiwary, B. Kim, L. Zhu, N. Chopra, I. N. Odeh, R. Vajtai, A. Z. Yu, R. Luo, J. Lou, G. Ding, P. J. A. Kenis, P. M. Ajayan, *Nat. Commun.* **2016**, *7*, 13869.
- [134] Y. Liu, Y. Zhang, A. Cheng, X. Quan, X. Fan, Y. Su, S. Chen, H. Zhao, Y. Zhang, H. Yu, M. R. Hoffmann, *Angew. Chem., Int. Ed.* **2017**, *56*, 15607.
- [135] Y. Liu, S. Chen, X. Quan, H. Yu, *J. Am. Chem. Soc.* **2015**, *137*, 11631.
- [136] J. J. Carroll, J. D. Slupsky, A. E. Mather, *J. Phys. Chem. Ref. Data* **1991**, *20*, 1201.
- [137] D. Kopljar, A. Inan, P. Vindayer, N. Wagner, E. Klemm, *J. Appl. Electrochem.* **2014**, *44*, 1107.
- [138] E. J. Dufek, T. E. Lister, M. E. Mcllwain, *Electrochem. Solid-State Lett.* **2012**, *15*, B48.
- [139] M. M. Monroe, P. Lobaccaro, Y. Lum, J. W. Ager, *J. Phys. D: Appl. Phys.* **2017**, *50*, 154006.
- [140] X. Lu, D. Y. C. Leung, H. Wang, M. M. Maroto-Valer, J. Xuan, *Renewable Energy* **2016**, *95*, 277.
- [141] D. V. Esposito, *Joule* **2017**, *1*, 651.
- [142] X. Lu, D. Y. C. Leung, H. Wang, J. Xuan, *Appl. Energy* **2017**, *194*, 549.
- [143] S. Verma, Y. Hamasaki, C. Kim, W. Huang, S. Lu, H.-R. M. Jhong, A. A. Gewirth, T. Fujigaya, N. Nakashima, P. J. A. Kenis, *ACS Energy Lett.* **2018**, *3*, 193.
- [144] C. E. Tornow, M. R. Thorson, S. Ma, A. A. Gewirth, P. J. A. Kenis, *J. Am. Chem. Soc.* **2012**, *134*, 19520.
- [145] H.-R. M. Jhong, C. E. Tornow, B. Smid, A. A. Gewirth, S. M. Lyth, P. J. A. Kenis, *ChemSusChem* **2017**, *10*, 1094.
- [146] C. M. Gabardo, A. Seifitokaldani, J. P. Edwards, C.-T. Dinh, T. Burdyny, M. G. Kibria, C. P. O'Brien, E. H. Sargent, D. Sinton, *Energy Environ. Sci.* **2018**, *11*, 2531.
- [147] H. R. Q. Jhong, F. R. Brushett, P. J. A. Kenis, *Adv. Energy Mater.* **2013**, *3*, 589.
- [148] S. Ma, Y. Lan, G. M. J. Perez, S. Moniri, P. J. A. Kenis, *ChemSusChem* **2014**, *7*, 866.
- [149] D. Kopljar, N. Wagner, E. Klemm, *Chem. Eng. Technol.* **2016**, *39*, 2042.
- [150] A. Del Castillo, M. Alvarez-Guerra, J. Solla-Gullón, A. Sáez, V. Montiel, A. Irabien, *J. CO<sub>2</sub> Util.* **2017**, *18*, 222.
- [151] C. Liang, B. Kim, S. Yang, Y. Liu, C. Francisco Woellner, Z. Li, R. Vajtai, W. Yang, J. Wu, P. J. A. Kenis, P. M. Ajayan, *J. Mater. Chem. A* **2018**, *6*, 10313.
- [152] T. T. H. Hoang, S. Ma, J. I. Gold, P. J. A. Kenis, A. A. Gewirth, *ACS Catal.* **2017**, *7*, 3313.
- [153] S. Ma, M. Sadakiyo, R. Luo, M. Heima, M. Yamauchi, P. J. A. Kenis, *J. Power Sources* **2016**, *301*, 219.
- [154] E. J. Dufek, T. E. Lister, S. G. Stone, M. E. Mcllwain, *J. Electrochem. Soc.* **2012**, *159*, F514.
- [155] K. Hara, A. Kudo, T. Sakata, M. Watanabe, *J. Electrochem. Soc.* **1995**, *142*, L57.
- [156] K. Hara, S. Tadayoshi, *J. Electrochem. Soc.* **1997**, *144*, 539.
- [157] E. J. Dufek, T. E. Lister, M. E. Mcllwain, *J. Appl. Electrochem.* **2011**, *41*, 623.
- [158] K. Hara, T. Sakata, *Bull. Chem. Soc. Jpn.* **1997**, *70*, 571.
- [159] P. Jeanty, C. Scherer, E. Magori, K. Wiesner-Fleischer, O. Hinrichsen, M. Fleischer, *J. CO<sub>2</sub> Util.* **2018**, *24*, 454.
- [160] W. Lee, Y. E. Kim, M. H. Youn, S. K. Jeong, K. T. Park, *Angew. Chem.* **2018**, *130*, 6999.
- [161] S. Shironita, K. Karasuda, M. Sato, M. Umeda, *J. Power Sources* **2013**, *228*, 68.
- [162] S. Shironita, K. Karasuda, K. Sato, M. Umeda, *J. Power Sources* **2013**, *240*, 404.
- [163] B. C. Marepally, C. Ampelli, C. Genovese, T. Saboo, S. Perathoner, F. M. Visser, L. Veyre, J. Canivet, E. A. Quadrelli, G. Centi, *ChemSusChem* **2017**, *10*, 4442.
- [164] D. Sebastián, A. Palella, V. Baglio, L. Spadaro, S. Siracusano, P. Negro, F. Niccoli, A. S. Aricò, *Electrochim. Acta* **2017**, *241*, 28.
- [165] M. Gangeri, S. Perathoner, S. Caudo, G. Centi, J. Amadou, D. Bégin, C. Pham-Huu, M. J. Ledoux, J. P. Tessonier, D. S. Su, R. Schlögl, *Catal. Today* **2009**, *143*, 57.
- [166] C. Genovese, C. Ampelli, S. Perathoner, G. Centi, *J. Catal.* **2013**, *308*, 237.
- [167] G. Centi, S. Perathoner, G. Winè, M. Gangeri, *Green Chem.* **2007**, *9*, 671.
- [168] C. Ampelli, C. Genovese, M. Errahali, G. Gatti, L. Marchese, S. Perathoner, G. Centi, *J. Appl. Electrochem.* **2015**, *45*, 701.
- [169] C. Jiménez, J. García, R. Camarillo, F. Martínez, J. Rincón, *Energy Fuels* **2017**, *31*, 3038.
- [170] I. Merino-Garcia, J. Albo, A. Irabien, *Nanotechnology* **2018**, *29*, 014001.
- [171] D. W. Dewulf, A. J. Bard, *Catal. Lett.* **1988**, *1*, 73.
- [172] C. Delacourt, P. L. Ridgway, J. B. Kerr, J. Newman, *J. Electrochem. Soc.* **2008**, *155*, B42.
- [173] G. Wang, J. Pan, S. P. Jiang, H. Yang, *J. CO<sub>2</sub> Util.* **2018**, *23*, 152.
- [174] S. Komatsu, M. Tanaka, A. Okumura, A. Kungi, *Electrochim. Acta* **1995**, *40*, 745.
- [175] L. M. Aeshala, S. U. Rahman, A. Verma, *Sep. Purif. Technol.* **2012**, *94*, 131.
- [176] L. M. Aeshala, R. G. Uppaluri, A. Verma, *J. CO<sub>2</sub> Util.* **2013**, *3–4*, 49.
- [177] L. M. Aeshala, R. Uppaluri, A. Verma, *Phys. Chem. Chem. Phys.* **2014**, *16*, 17588.
- [178] Z. Liu, R. I. Masel, Q. Chen, R. Kutz, H. Yang, K. Lewinski, M. Kaplun, S. Luopa, D. R. Lutz, *J. CO<sub>2</sub> Util.* **2016**, *15*, 50.
- [179] R. B. Kutz, Q. Chen, H. Yang, S. D. Sajjad, Z. Liu, I. R. Masel, *Energy Technol.* **2017**, *5*, 929.
- [180] M. B. McDonald, S. Ardo, N. S. Lewis, M. S. Freund, *ChemSusChem* **2014**, *7*, 3021.
- [181] S. Chabi, A. G. Wright, S. Holdcroft, M. S. Freund, *ACS Appl. Mater. Interfaces* **2017**, *9*, 26749.
- [182] J. Luo, D. A. Vermaas, D. Bi, A. Hagfeldt, W. A. Smith, M. Grätzel, *Adv. Energy Mater.* **2016**, *6*, 1600100.
- [183] K. Sun, R. Liu, Y. Chen, E. Verlage, N. S. Lewis, C. Xiang, *Adv. Energy Mater.* **2016**, *6*, 1600379.
- [184] R. S. Reiter, W. White, S. Ardo, *J. Electrochem. Soc.* **2016**, *163*, H3132.
- [185] Y. C. Li, D. Zhou, Z. Yan, R. H. Gonçalves, D. A. Salvatore, C. P. Berlinguette, T. E. Mallouk, *ACS Energy Lett.* **2016**, *1*, 1149.
- [186] D. A. Salvatore, D. M. Weekes, J. He, K. E. Dettelbach, Y. C. Li, T. E. Mallouk, C. P. Berlinguette, *ACS Energy Lett.* **2017**, *3*, 149.
- [187] Y. C. Li, Z. Yan, J. Hitt, R. Wycisk, P. N. Pintar, T. E. Mallouk, *Adv. Sustainable Syst.* **2018**, *2*, 1700187.
- [188] L. Zhang, S. Hu, X. Zhu, W. Yang, *J. Energy Chem.* **2017**, *26*, 593.
- [189] X. Zhang, Y. Song, G. Wang, X. Bao, *J. Energy Chem.* **2017**, *26*, 839.
- [190] R. J. Lim, M. Xie, M. A. Sk, J. M. Lee, A. Fisher, X. Wang, K. H. Lim, *Catal. Today* **2014**, *233*, 169.
- [191] S. D. Ebbesen, S. H. Jensen, A. Hauch, M. B. Mogensen, *Chem. Rev.* **2014**, *114*, 10697.
- [192] B. Kim, F. Hillman, M. Ariyoshi, S. Fujikawa, P. J. A. Kenis, *J. Power Sources* **2016**, *312*, 192.
- [193] L. Cindrella, A. M. Kannan, J. F. Lin, K. Saminathan, Y. Ho, C. W. Lin, J. Wertz, *J. Power Sources* **2009**, *194*, 146.
- [194] A. Li, H. Wang, J. Han, L. Liu, *Front. Chem. Sci. Eng.* **2012**, *6*, 381.
- [195] N. P. Brandon, D. J. Brett, *Philos. Trans. R. Soc. A* **2006**, *364*, 147.
- [196] Q. Wang, H. Dong, H. Yu, *RSC Adv.* **2014**, *4*, 59970.
- [197] J. Wu, P. P. Sharma, B. H. Harris, X. D. Zhou, *J. Power Sources* **2014**, *258*, 189.
- [198] Q. Wang, H. Dong, H. Yu, H. Yu, *J. Power Sources* **2015**, *279*, 1.
- [199] S. Ma, J. Liu, K. Sasaki, S. M. Lyth, P. J. A. Kenis, *Energy Technol.* **2017**, *5*, 861.
- [200] Q. Wang, H. Dong, H. Yu, *J. Power Sources* **2014**, *271*, 278.
- [201] J. Lee, R. Yip, P. Antonacci, N. Ge, T. Kotaka, Y. Tabuchi, A. Bazylak, *J. Electrochem. Soc.* **2015**, *162*, F669.

- [202] A. S. Agarwal, Y. Zhai, D. Hill, N. Sridhar, *ChemSusChem* **2011**, *4*, 1301.
- [203] S. Sen, B. Skinn, T. Hall, M. Inman, E. J. Taylor, F. R. Brushett, *MRS Adv.* **2017**, *2*, 451.
- [204] S. Verma, X. Lu, S. Ma, R. I. Masel, P. J. A. Kenis, *Phys. Chem. Chem. Phys.* **2016**, *18*, 7075.
- [205] N. Gutiérrez-Guerra, L. Moreno-López, J. C. Serrano-Ruiz, J. L. Valverde, A. de Lucas-Consuegra, *Appl. Catal. B* **2016**, *188*, 272.
- [206] B. A. Rosen, A. Salehi-Khojin, M. R. Thorson, W. Zhu, D. T. Whipple, P. J. A. Kenis, R. I. Masel, *Science* **2011**, *334*, 643.
- [207] L. Sun, G. K. Ramesha, P. V. Kamat, J. F. Brennecke, *Langmuir* **2014**, *30*, 6302.
- [208] J. Li, G. Prentice, *J. Electrochem. Soc.* **1997**, *144*, 4284.
- [209] S. Kaneco, K. Iiba, H. Katsumata, T. Suzuki, K. Ohta, *Electrochim. Acta* **2006**, *51*, 4880.
- [210] P. P. Sharma, X.-D. Zhou, *Wiley Interdiscip. Rev.: Energy Environ.* **2017**, *6*, e239.
- [211] Y. Wang, J. Liu, Y. Wang, A. M. Al-Enizi, G. Zheng, *Small* **2017**, *13*, 1701809.
- [212] J.-P. Jones, G. K. S. Prakash, G. A. Olah, *Isr. J. Chem.* **2014**, *54*, 1451.
- [213] N. Gupta, M. Gattrell, B. MacDougall, *J. Appl. Electrochem.* **2006**, *36*, 161.
- [214] S. Ma, R. Luo, S. Moniri, Y. Lan, P. J. A. Kenis, *J. Electrochem. Soc.* **2014**, *161*, F1124.
- [215] B. Kim, S. Ma, H. R. Molly Jhong, P. J. A. Kenis, *Electrochim. Acta* **2015**, *166*, 271.
- [216] O. Scialdone, A. Galia, G. Lo Nero, F. Proietto, S. Sabatino, B. Schiavo, *Electrochim. Acta* **2016**, *199*, 332.
- [217] D. T. Whipple, E. C. Finke, P. J. A. Kenis, *Electrochem. Solid-State Lett.* **2010**, *13*, B109.
- [218] A. S. Varela, M. Kroschel, T. Reier, P. Strasser, *Catal. Today* **2016**, *260*, 8.
- [219] A. Murata, Y. Hori, *Bull. Chem. Soc. Jpn.* **1991**, *64*, 123.
- [220] R. Kas, R. Kortlever, H. Yilmaz, M. T. M. Koper, G. Mul, *ChemElectroChem* **2015**, *2*, 354.
- [221] J. Resasco, Y. Lum, E. Clark, J. Z. Zeledon, A. T. Bell, *ChemElectroChem* **2018**, *5*, 1064.
- [222] Y. Hori, S. Suzuki, *Bull. Chem. Soc. Jpn.* **1982**, *55*, 660.
- [223] J. Resasco, L. D. Chen, E. Clark, C. Tsai, C. Hahn, T. F. Jaramillo, K. Chan, A. T. Bell, *J. Am. Chem. Soc.* **2017**, *139*, 11277.
- [224] M. R. Thorson, K. I. Siil, P. J. A. Kenis, *J. Electrochem. Soc.* **2013**, *160*, F69.
- [225] G. Z. Kyriacou, A. K. Anagnostopoulos, *J. Appl. Electrochem.* **1993**, *23*, 1196.
- [226] S. Kaneco, H. Katsumata, T. Suzuki, K. Ohta, *Energy Fuels* **2006**, *20*, 409.
- [227] S. Kaneco, H. Katsumata, T. Suzuki, K. Ohta, *Electrochim. Acta* **2006**, *51*, 3316.
- [228] M. R. Singh, Y. Kwon, Y. Lum, J. W. Ager, A. T. Bell, *J. Am. Chem. Soc.* **2016**, *138*, 13006.
- [229] J. Wu, F. G. Risalvato, F.-S. Ke, P. J. Pellechia, X.-D. Zhou, *J. Electrochem. Soc.* **2012**, *159*, F353.
- [230] A. S. Varela, W. Ju, T. Reier, P. Strasser, *ACS Catal.* **2016**, *6*, 2136.
- [231] R. J. Gilliam, J. W. Graydon, D. Kirk, S. J. Thorpe, *Int. J. Hydrogen Energy* **2007**, *32*, 359.
- [232] R. C. Weast, *CRC Handbook of Chemistry and Physics*, 70th Edition, CRC Press, Inc., Boca Raton, FL, USA **1989**.
- [233] E. J. Dufek, T. E. Lister, S. G. Stone, *J. Appl. Electrochem.* **2014**, *44*, 849.
- [234] K. Hara, A. Kudo, T. Sakata, *J. Electroanal. Chem.* **1995**, *391*, 141.
- [235] K. Hara, A. Tsuneto, A. Kudo, T. Sakata, *J. Electrochem. Soc.* **1994**, *141*, 2097.
- [236] T. Saeki, K. Hashimoto, N. Kimura, K. Omata, A. Fujishima, *J. Electroanal. Chem.* **1996**, *404*, 299.
- [237] M. Todoroki, K. Hara, A. Kudo, T. Sakata, *J. Electroanal. Chem.* **1995**, *394*, 199.
- [238] F. Köleli, D. Balun, *Appl. Catal. A: Gen.* **2004**, *274*, 237.
- [239] F. Proietto, B. Schiavo, A. Galia, O. Scialdone, *Electrochim. Acta* **2018**, *277*, 30.
- [240] S. Nakagawa, A. Kudo, M. Azuma, T. Sakata, *J. Electroanal. Chem. Interfacial Electrochem.* **1991**, *308*, 339.
- [241] A. Kudo, S. Nakagawa, A. Tsuneto, T. Sakata, *J. Electrochem. Soc.* **1993**, *140*, 1541.
- [242] K. Hara, A. Kudo, T. Sakata, *J. Electroanal. Chem.* **1997**, *421*, 1.
- [243] Y. Hori, A. Murata, *Electrochim. Acta* **1990**, *35*, 1777.
- [244] R. Kas, K. K. Hummadi, R. Kortlever, P. de Wit, A. Milbrat, M. W. J. Luiten-Olieman, N. E. Benes, M. T. M. Koper, G. Mul, *Nat. Commun.* **2016**, *7*, 10748.
- [245] H. De Jesús-Cardona, C. del Moral, C. R. Cabrera, *J. Electroanal. Chem.* **2001**, *513*, 45.
- [246] EG&G Technical Services, *Fuel Cell Handbook*, 7th ed., US Department of Energy, Morgantown, WV **2004**.
- [247] A. J. Martín, G. O. Larrazábal, J. Pérez-Ramírez, *Green Chem.* **2015**, *17*, 5114.
- [248] M. J. Morans, H. N. Shapiro, D. D. Boettner, M. B. Bailey, *Fundamentals of Engineering Thermodynamics*, John Wiley & Sons, Inc., Hoboken, NJ **2014**.
- [249] J. Kestin, M. Sokolov, W. A. Wakeham, *J. Phys. Chem. Ref. Data* **1978**, *7*, 941.
- [250] E. N. Fuller, P. D. Schettler, J. C. Giddings, *Ind. Eng. Chem.* **1966**, *58*, 18.
- [251] M. Azuma, K. Hashimoto, M. Hiramoto, M. Watanabe, T. Sakata, *J. Electroanal. Chem. Interfacial Electrochem.* **1989**, *260*, 441.
- [252] M. Azuma, K. Hashimoto, M. Watanabe, T. Sakata, *J. Electroanal. Chem. Interfacial Electrochem.* **1990**, *294*, 299.
- [253] S. Kaneco, N. Hiei, Y. Xing, H. Katsumata, H. Ohnishi, T. Suzuki, K. Ohta, *J. Solid State Electrochem.* **2003**, *7*, 152.
- [254] S. T. Ahn, I. Abu-Baker, G. T. R. Palmore, *Catal. Today* **2017**, *288*, 24.
- [255] M. Azuma, K. Hashimoto, M. Hiramoto, M. Watanabe, S. Tadayoshi, *J. Electrochem. Soc.* **1990**, *137*, 1772.
- [256] S. Kaneco, N. Hiei, Y. Xing, H. Katsumata, H. Ohnishi, T. Suzuki, K. Ohta, *Electrochim. Acta* **2002**, *48*, 51.
- [257] Y. Hori, K. Kikuchi, A. Murata, S. Suzuki, *Chem. Lett.* **1986**, *15*, 897.
- [258] R. L. Cook, *J. Electrochem. Soc.* **1988**, *135*, 1320.
- [259] J. J. Kim, D. P. Summers, K. W. Frese, *J. Electroanal. Chem. Interfacial Electrochem.* **1988**, *245*, 223.
- [260] Y. Ougitani, T. Aizawa, N. Sonoyama, T. Sakata, *Bull. Chem. Soc. Jpn.* **2001**, *74*, 2119.
- [261] T. Mizuno, K. Ohta, A. Sasaki, T. Akai, M. Hirano, A. Kawabe, *Energy Sources* **1995**, *17*, 503.
- [262] S. M. A. Kriescher, K. Kugler, S. S. Hosseiny, Y. Gendel, M. Wessling, *Electrochem. Commun.* **2015**, *50*, 64.
- [263] N. Gutiérrez-Guerra, J. L. Valverde, A. Romero, J. C. Serrano-Ruiz, A. de Lucas-Consuegra, *Electrochem. Commun.* **2017**, *81*, 128.
- [264] T. Li, Y. Cao, J. He, C. P. Berlinguette, *ACS Cent. Sci.* **2017**, *3*, 778.